
# Chemical bath deposition of $Zn_{1-x}Sn_xO_y$ films as buffer layers for $Cu(In,Ga)Se_2$ solar cells

by

Diego Alejandro Garzón Castellanos

**Supervisors:** Sascha Sadewasser, PhD.

Diego Colombara, PhD.

July 2022

**Table of Contents**

**Abstract**

Climate change is among the most critical issues challenging humanity. Through the direct conversion of solar energy into electricity, photovoltaics is a viable response to this challenge. Specifically, $Cu(In,Ga)Se_2$ (CIGSe) thin-film solar cells are a commercial photovoltaic technology that provides sustainable energy production. Therefore, we studied the formation of $Zn_{1-x}Sn_xO_y$ (ZTO) thin-films as Cd-free buffer layers by chemical bath deposition (CBD). The latter were obtained by exploring the effect of each deposition parameter onto the morphology, crystal structure, and optical properties of columnar ZnO. We observed that increasing pH or complexing agent concentration slows down the deposition process, while a decrease in Zn cation concentration is related to a lower homogeneity of the films. Later, ZTO films were obtained with a flatter morphology related to the inhibition of columnar growth. In addition, a non-trivial increase of the band gap was observed with increasing Sn concentration. Then, the buffer layer was grown on industry-grade CIGSe absorbers, which led to a similar performance to the CdS-based solar cell. We obtained a maximum efficiency of 11% (5% higher than the CdS-based reference), related to high open-circuit voltage and fill factor.

**Resumo**

As alterações climáticas estão entre as questões mais críticas que desafiam a sobrevivência da humanidade. Através da conversão direta da energia solar em eletricidade, a tecnologia fotovoltaica é uma resposta viável a este desafio. Especificamente, as células solares de filme fino de $Cu(In,Ga)Se_2$ (CIGSe) são uma tecnologia fotovoltaica comercial que possibilita a produção de energia de forma sustentável. Assim sendo, estudámos a formação de filmes finos de $Zn_{1-x}Sn_xO_y$ (ZTO) como camada tampão (*buffer)* livre de Cd por deposição química em banho (CBD). Estudámos os efeitos de cada parâmetro de deposição na morfologia, estrutura cristalina e propriedades óticas do ZnO colunar. Observou-se que o aumento do pH ou concentração de agentes complexantes retarda o processo de deposição, enquanto uma diminuição da concentração de catiões do Zn está relacionada com uma menor homogeneidade dos filmes. Em seguida, os filmes de ZTO foram obtidas com uma morfologia mais plana relacionada com a inibição do crescimento colunar. Além disso, foi observado um aumento não trivial do hiato com o aumento da concentração de Sn. Depois, a camada tampão (*buffer)* foi depositada em absorvedores CIGSe comerciais, o que levou a um desempenho semelhante ao da célula com CdS. Além disso, obtivemos uma eficiência máxima de 11% (5% superior à referência de CdS), relacionada com uma alta tensão de circuito aberto e *fill factor*.

**Symbols and abbreviations**

| | |
|---|---|
| ALD | Atomic layer deposition |
| BFDH | Bravais, Friedel, Donnay and Harker |
| CBD | Chemical bath deposition |
| CBO | Conduction band offset |
| CIGSe | $Cu(In,Ga)Se_2$ |
| DIW | Deionized water |
| DSSCs | Dye-sensitized solar cells |
| EA | Ethanolamine |
| $E_C$ | Energy of the conduction band |
| EDX | Energy-dispersive X-ray spectroscopy |
| $E_{g,p}$ | Absorber band gap |
| $E_{g,n}$ | Buffer band gap |
| $E_F$ | Fermi energy |
| $E_V$ | Energy of the valence band |
| EQE | External quantum efficiency |
| FF | Fill factor |
| $J_{sc}$ | Short-circuit current density |
| JV | Current density – voltage |
| PCE | Power conversion efficiency |
| PV | Photovoltaic |
| $R_{series}$ | Series resistance |
| $R_{shunt}$ | Shunt resistance |
| SEM | Scanning electron microscopy |
| SLG | Soda-lime glass |
| STAR | Sputtering for Advanced Research |
| TTZ | [Sn]/([Sn]+[Zn]) ratio |
| UV-VIS-NIR | Ultraviolet, visible and near infrared |
| $V_{oc}$ | Open-circuit voltage |
| XPS | X-Ray Photoelectron Spectroscopy |
| XRD | X-ray diffraction |
| ZTO | Zinc tin oxide, $Zn_{1-x}Sn_xO_y$ |

## 1. Introduction

Nowadays, society is facing several challenges related to health, education, energy, security, and climate change, among others. Even though all these issues are pressing, energy provision concerns several sectors directly or indirectly, from medicine, business, and agriculture, to industry and education.[1] Therefore, the development of innovative and renewable ways to harvest energy is an urgent need for humankind. That is why the United Nations has defined clean energy development as one of the 17 sustainable development goals[1], and many nations and international organizations are following these guidelines, making energy research a priority.[2–4]

For a long time, fossil fuels have been (and still are) a major driver of the energy market. However, burning fossil fuels causes environmental and health problems that affect everyone. Specifically, three-quarters of global greenhouse gas emission are related to the burning of fossil fuels, and it is estimated that five million casualties worldwide each year are caused by air pollution.[5] A fast transition to cleaner energy technologies has become a priority. Yet, in the last twenty years, the use of renewable energies has only increased from 18.5% to 28.3% of the global energy supply, representing a global growth of around 0.5 percentage points per year.[5]

Among the various renewable energy sources, hydropower represents the lion's share, followed by wind and solar.[5] Hydropower plants and wind farms operate by harvesting the potential energy of water and the movement of air currents.[6] It is worth mentioning that both hydro and wind energies have historical roots dating back to pre-industrial age (irrigation mechanisms, wind-based transportations in ancient civilizations, as well as water/wind mills at least since the middle ages), and still represent a large portion of the low-carbon energy sources.

The conversion of solar radiation into usable power showed the most remarkable enhancement over the last 2 decades. Even though solar technologies represents less than 2% of the global energy supply, their use has grown exponentially over the previous 35 years because the power conversion efficiency (PCE, defined as the ratio of power output to incident sunlight power) has increased, whereas the manufacturing costs keep decreasing as the market expands.[5,6]

There are two ways to harvest the energy irradiated by the sun: converting it into heat or by directly converting it into electricity. Photovoltaic (PV) devices offer a way to obtain electricity directly via exposure to sunlight.[6] In simple terms, PV devices are composed of semiconductor layers that form a p-n junction, together with two electrodes, back and front contact, to collect the generated electricity. In addition, other layers are often added to boost the performance and stability of the solar cell.

Several generations of PV have been developed over the years. The first-generation PV technology is represented by crystalline silicon solar cells, which is still the dominant technology in the market.[7] The second-generation PV technology refers to the thin-film solar cells that include direct bandgap semiconductors such as cadmium telluride (CdTe), amorphous silicon, and copper indium gallium diselenide (CIGSe).[8] Lastly, the third-generation PV technology corresponds to emerging concepts based on organometallic materials (dye-sensitized solar cells) and perovskites materials, together with multijunction, tandem and hot carrier technologies.[6,9–11]

Technologies like the thin-film solar cells entail the deposition of varied materials in the form of layers with thickness in the range from micro- to nanometers. In particular, the thickness of

the layers responsible for light absorption is lower than in the case of crystalline silicon solar cells. As a consequence, thin-film solar cells generally present an opportunity for flexible, tandem or semi-transparent applications, together with easy manufacturing for large area module arrays and simple device processing in terms of deposition temperature, compared with silicon solar cells.[8,12] Among thin-film technologies, CIGSe has been widely studied because it can be prepared by several methods that give high control to its properties, notably its tunable band gap (1.0 – 1.7 eV)[10,13], and high absorption coefficient (>$10^5$ $cm^{-1}$)[10,13] with final record PCE up to 23.4% achieved by SolarFrontier.[14] Nevertheless, these technologies have drawbacks, such as the limited availability on the Earth's crust of some of the raw materials required.[9] Figure 1 shows the historical progress of the PCE for the thin-film PV technologies.[15]

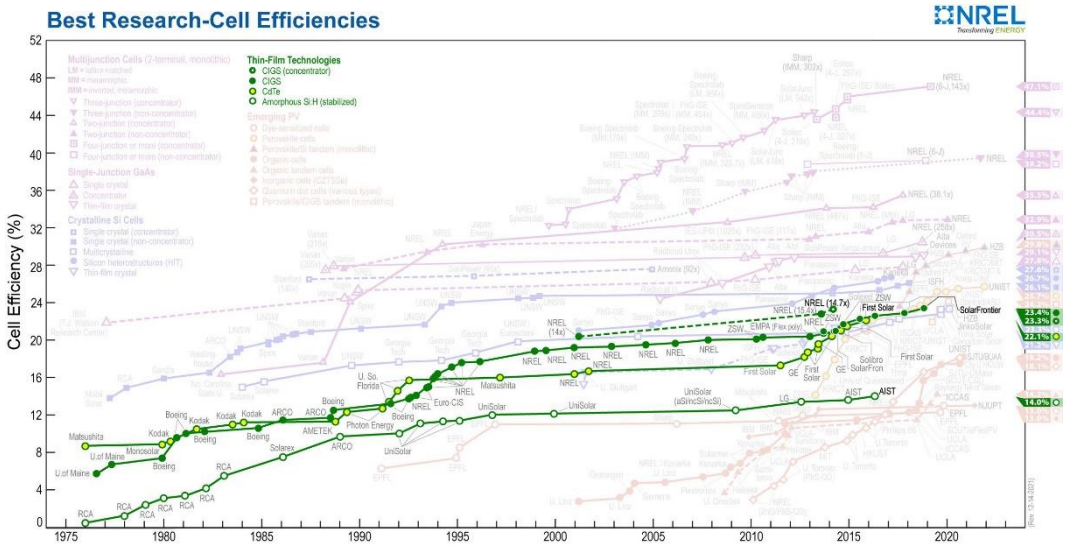


*Figure 1. Highest confirmed PCE for research cells for a range of photovoltaic technologies plotted versus the year, focused on the thin-film technologies.* [15]

PVs cells are based on a p-n junction formed at the interface between two semiconductors, with excess of holes and electrons on the p and n side, respectively. Considering the photovoltaic effect, when the light interacts with the p side (the absorber in the case of CIGSe technology), electrons from the valence band get promoted to the conduction band, forming an electron-hole pair. These electrons, move to the n side, due to the electromotive force produced by the p-n junction, while the holes move to the opposite side of the solar cell. This charge separation produces a current in an external circuit.[6,16,17] Figure 2b shows the ideal current generation process when a photon interacts with the absorber.

Nevertheless, not all the light interacting with the solar cell is converted into electricity. Some intrinsic and extrinsic effects that contribute to PCE losses.[17,18] An interesting intrinsic effect can be described in terms of photon energy because only the photons with higher or equal energy as the absorber band gap ($E_{g,p}$) can produce electron-hole pairs. In addition, the pairs generated by those with greater energy ($h\nu > E_{g,p}$) experience an energy loss due to thermalization to the conduction band edge.[19]

Furthermore, electrons in the conduction band can recombine with holes in the valence band producing energy as light or heat with a resulting decrease in solar cell's PCE. There are three different recombination pathways: Radiative, defective and Auger. In the radiative case, the electron-hole recombination causes the emission of a photon.[17] In the defective mechanism, an intermediate energy state is present due to a defect or impurity in the material that traps

electrons or holes, dissipating energy in the form of phonons.[20,21] Lastly, Auger recombination involves three particles, after the electron-hole recombination an electron in the conduction band gets excited and further thermalized back to the band edge.[17]

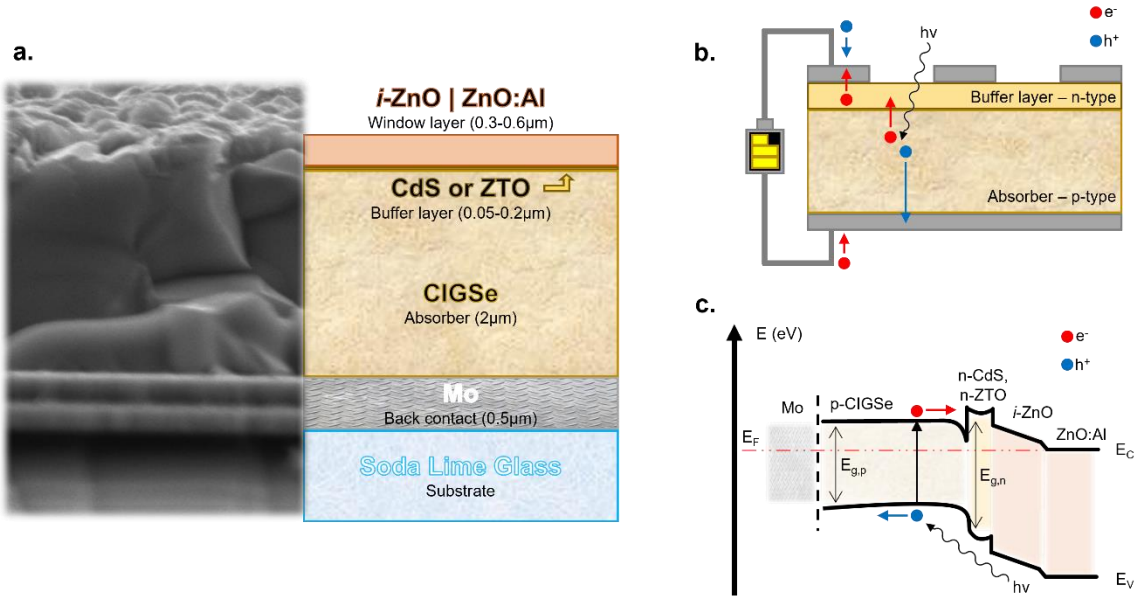


*Figure 2. (a) Structure of a CIGSe-based solar cell. (b) Working principle of solar cells, showing the photovoltaic effect in a p-n junction. (c) Scheme of a band diagram of a CIGSe-based solar cell.*

Figure 2a shows a general structure for CIGSe solar cells, and a cross section image collected with scanning electron microscopy (SEM). The CIGSe solar cell architecture is composed of a molybdenum back contact deposited on a soda-lime glass (SLG) substrate, onto which the CIGSe layer (also called absorber) is deposited. The CIGSe absorber layer is responsible for light absorption and, together with the buffer layer, it forms the p-n junction. Historically, several materials have been employed as buffer layers, the most common buffer is cadmium sulfide, while zinc oxide or sulfide derivatives are emerging.[22–24] Finally, the solar cell has a window layer made of intrinsic ZnO or ZnMgO and aluminum-doped ZnO. In this case, the ZnMgO works as an insulator to decrease the recombination probability, while the conductive aluminum-doped ZnO works as the front contact.[25]

The role of the buffer is decisive in obtaining high-efficiency cells; this layer should provide a good electrical and optical interface with both absorber and front contact layers to obtain an adequate charge carrier transport and decrease the interface recombination. Figure 2c shows a band diagram for the CIGSe solar cell. Here, the conduction band minimum of the buffer layer is higher than that of the absorber (thus, giving a positive conduction band offset, CBO) to minimize interface recombination by inducing n-type conversion of the CIGSe surface.[26]

CdS is the traditional buffer material due to its electrical and structural matching with the absorber.[27] Nevertheless, its relatively low direct band gap, $E_g$ = 2.4-2.5 eV[28], prevents high energy photons from being absorbed by the p-CIGSe.[22] In addition, the presence of the highly toxic Cd presents several health and environmental concerns.[29,30] Therefore, a wider band gap and less toxic materials have been researched to produce Cd-free CIGSe solar cells.[22–24] Among these materials, zinc tin oxide ($Zn_{1-x}Sn_xO_y$, ZTO) has attracted much attention due to its non-toxicity, fast light responsivity, and tuneable wide band gap. CIGSe solar cells based on ZTO buffers resulted in PCE comparable to or even higher than CdS ones.[22,23,27,31]

However, until now, ZTO buffer layers have been fabricated by atomic layer deposition (ALD), a hardly scalable, time-consuming, and expensive technique. In contrast, CdS thin-films are obtained by chemical bath deposition (CBD), which is a fast, reliable, cheap, batch-scalable, low temperature (<100 °C) technique that allows conformal growth.[32–34]

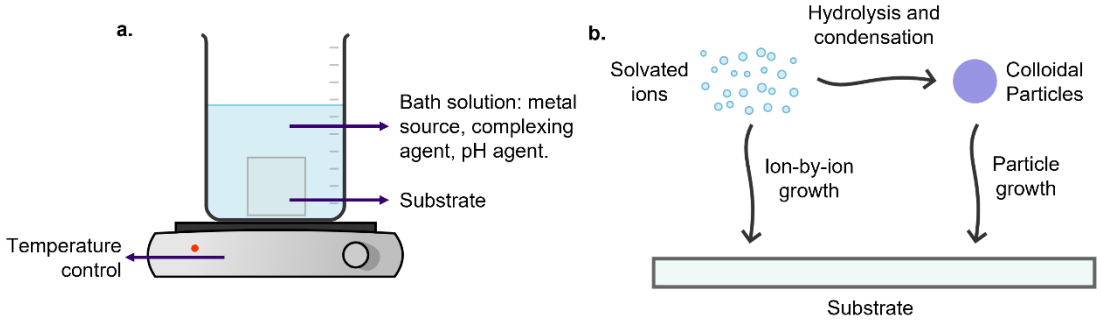


*Figure 3. (a) General experimental setup for a chemical bath deposition (CBD). (b) Mechanisms proposed for the films formation via CBD.*

CBD is a technique that consists in the deposition of inorganic (oxide, sulfide, or selenide) thin-films by immersion of the substrate in a precursor solution. It is based on a controlled chemical reaction -normally a hydrolysis- in solution -typically aqueous- that results in either homogenous or heterogonous nucleation on the substrate. Figure 3a shows a general setup for the CBD. Generally, the precursor aqueous solution involves a soluble metal salt, a pH agent, and a complexing agent, used to control the hydrolysis rate.[35] In addition, ions should be in a metastable supersaturated state to let the reaction take place. In these circumstances there is almost no bulk precipitation because the solid forms on the surface of any substrate, since surfaces lower the thermodynamic barrier for nucleation. Therefore, two mechanisms have been proposed for forming thin-films by CBD: ion-by-ion growth and particle growth, shown in Figure 3b. In the first case, heterogenous nucleation leads to the direct growth of nuclei onto the substrate. While in the second situation, colloidal particles form in solution and subsequently adhere to the substrate leading to particle growth. These mechanisms may occur exclusively, simultaneously or sequentially, depending on the interactions occurring in each system.[35]

Studies on CBD for ZnO thin-films have shown diverse nanostructured morphologies such as columnar grains, rods, stars or spherical habits, etc., obtained by tuning parameters such as ligands, counter-ions of the metal salts, pH, temperature, and nature of the substrate.[36,37] Furthermore, the electrical and optical properties of ZnO thin-films have also been modified by doping with other metals such as aluminum, gallium, indium, tin, etc.[38] Hence, the CBD of ZnO lends itself to relatively simple modifications in the bath, substrate or temperature to tune the thin-film composition and properties. The latter, represents a useful starting point for the growth of ZTO thin-films by CBD.

This study investigates the deposition of ZTO thin-films by CBD on several substrates and its applications as a buffer layer for CIGSe-based solar cells. First, an optimization of the deposition of ZnO thin-films was performed by analyzing the effect of pH, complexing agent, metal source concentration, and temperature. Subsequently, these films were doped with Sn, to understand the effect of these cations. Lastly, the current density - voltage (JV) characteristics of solar cell devices based on ZTO buffer layers were measured and compared with the CdS-based ones.

## 2. Materials and methods

### 2.1. Deposition of zinc oxide thin-films onto soda-lime glass substrates (SLG)

The zinc oxide thin-films were deposited onto SLG by chemical bath deposition (CBD) based on the process reported by *Kokotov, et al.*[33] Consequently, the substrates were first cleaned by sonication with deionized water (DIW) and soap in a general batch. The substrates were then activated with a fresh solution of potassium permanganate (0.5 – 50 mM) and 25 µL of 1-butanol per 10 mL of solution at 85°C for 20 min. Next, the substrates were rinsed with DIW 10 times and sonicated with DIW for 20 min. The deposition bath was prepared by sequential addition of aliquots of the stock solutions of zinc sulphate heptahydrate 1.0 M, ammonium hydroxide ~4M, and ethanolamine 50% v/v in DIW. In this way, final concentrations in the range of 50 – 100 mM for $ZnSO_4$, 0.2 – 1.0 M for $NH_4OH$, and 0.8 – 2.4 M for ethanolamine were obtained. Upon solution preparation, the substrates were immediately immersed vertically, and the beaker was left in a water bath at 85-92°C for 10-60 minutes. It is worth mentioning that the thin-film properties were optimized by modifying the concentration of the reactants, together with the time and the temperature of the reaction.

The final optimized protocol consists of an activation with a 5 mM $KMnO_4$ solution and 1-butanol (25 µL per 10 mL of solution) at 85°C for 20 min, followed by a deposition in a bath with a final concentration of 75 mM $Zn^{2+}$,0.2 M $NH_4OH$, and 1.6 M ethanolamine at 92°C.

### 2.2. Deposition of zinc tin oxide (ZTO) thin films onto SLG and different substrates

After the optimization of the deposition of ZnO thin films by CBD, the tin source was added in a similar fashion. In a typical deposition, the substrate was cleaned, and then activated with a solution of 5 mM $KMnO_4$ and 1-butanol, following the procedure described in section 2.1. Next, the deposition bath was prepared by the consecutive addition of aliquots of $ZnSO_4$, $NH_4OH$, ethanolamine and $SnCl_2$ stock solutions to obtain a final concentration of 75 mM of cations ($[Zn^{2+}]+[Sn^{2+}]$), 0.2 M $NH_4OH$, and 1.6 M ethanolamine. Furthermore, the depositions were carried out at 92 °C with variation of the [Sn]/([Sn]+[Zn]) ratio (TTZ) for 10-70 min in a range of 0-50% TTZ. It is worth mentioning that the stock solution of tin(II) chloride 1.5 M was prepared in an acidic medium with enough concentrated HCl to obtain a translucid solution (~1.7 M HCl), the latter to prevent the hydrolysis and precipitation of tin hydroxides.

This procedure was run onto SLG to study how the Sn concentration influences the properties of the thin-films. Furthermore, the role of the substrate was investigated by performing the same CBD at 30% TTZ onto SLG/Mo, silicon wafer, quartz and CIGSe with and without the potassium permanganate activation.

### 2.3. Fabrication of thin-film solar cells

For the solar cell fabrication, NICE Solar Energy CIGSe absorbers were employed. Such absorbers are composed of a soda-lime glass substrate with a thin layer (500 nm) of molybdenum as back-contact and a layer of around 2-3 µm of CIGSe on top. First, the CIGSe was treated with a fresh 5 wt. % KCN solution for 1 min to remove any Cu-selenides.[39,40] Immediately after the etching, the buffer layer (CdS or ZTO) was deposited by CBD. In the case of 50 nm thick CdS deposition, a solution of 1.33 g of thiourea, 0.13 g of cadmium acetate, 15 ml of $NH_4OH$, and 115 ml of DIW was used.[41] The bath was prepared by the sequential addition of DIW, $NH_4OH$, $Cd(CH_3CO_2)_2$ and thiourea, it was set at 60 °C and the sample was

immersed into it for 7 min. For the ZTO buffer, the same protocol described in section 2.2 was used, but without activation of the substrate and with a deposition time of 30 min at 92°C. In this case, a range of 10 – 40 % TTZ was investigated.

To complete the solar cell, a double window layer was deposited by RF-sputtering at room temperature in the window chamber of the Sputtering for Advanced Research (STAR) system.[25] Firstly, an intrinsic ZnMgO layer was deposited at $6.1\times10^{-3}$ mbar Ar pressure with 50 W for 14 min (thickness around 20 nm). Next, an aluminum-doped ZnO layer was deposited at $4.0\times10^{-3}$ mbar Ar pressure with 59 W for 51.5 min (~300 nm).

### 2.4. Characterization of thin-films

The thin-film morphology was determined by top-view and cross-section micrographs obtained by scanning electron microscopy (SEM) in an FEI Quanta 50 FEG SEM. The optical transmittance of the thin-films on SLG was measured in the range of 250-1200 nm with a PerkinElmer LAMBDA 950 UV-VIS-NIR spectrophotometer coupled with an integrated sphere detector module. The optical bandgaps were determined by the Tauc method, where the band gap is equal to the abscissa of $(\alpha h\nu)^r$ as a function of photon energy ($h\nu$), with r=2 (for direct band gap materials), $\alpha=\log_{10}(T)/t$, with T= the measured transmittance, and t= the film thickness.[42] The thickness of the samples was assessed by contact profilometry with the Tencor P-16 Surface Profiler.

The crystal structure was determined by X-ray diffraction (XRD) using Cu Kα radiation in a Panalytical XPert PRO MRD. The XRD patterns, were processed in HighScore, and the patterns shown in this work are their Rietveld refinement.[43] In addition, the crystallite size was estimated with the Scherrer equation[44]: $D = K\cdot\lambda/(W\cdot\cos\theta_W)$, where K = 0.9 was used for the shape factor, $\lambda$ is the wavelength of the X-rays, and W the full width half maximum at the Bragg angle $\theta_W$. The chemical composition of the thin-films was determined by X-Ray photoelectron spectroscopy (XPS) with the ESCALAB 250Xi (Thermo Scientific). Firstly, an XPS survey was done followed by high-resolution surveys for C 1s, O 1s, Sn 3d, Zn 2p. Secondly, a 90s etching was done in an Ar atmosphere to study both the surface and inside the thin-film. Lastly, the peaks were fitted and the TTZ was determined with the areas related to the Zn $2p_{3/2}$ and Sn $3d_{5/2}$. It is worth mentioning that the C 1s peak (284.8 eV) was used as an internal standard.

### 2.5. Characterization of thin-film solar cells

The current density - voltage (JV) characteristics of solar cell devices were measured in a solar simulator (Oriel Sol3A class AAA) under AM1.5 illumination. Devices were manually scribed to ~0.15 $cm^2$ and measured without a front grid at room temperature. External quantum efficiency (EQE) was measured by the QEX10 Solar Cell Quantum Efficiency Measurement (PV measurement Inc.). A 75 W Xenon arc lamp was used as a white light source to generate monochromatic beam. The DC mode was used in a spectral range of 300–1100 nm.

## 3. Results and discussion

### 3.1. Optimization of the deposition of ZnO thin-films onto SLG

As reported by *Kokotov, et al.*[33] the homogeneous growth of ZnO requires an activation process onto the SLG substrates before the deposition.[33,45] Also in this study, no ZnO growth was observed in the non-activated SLG or in the SLG activated with $H_2O_2$, while the activation

treatment developed by the authors allowed the uniform growth of columns of ZnO.[33] The latter process exploits an aqueous solution of $KMnO_4$ mixed with 1-butanol which allows the formation of the nucleation agent Mn(O)OH by the oxidation of the alcohol. The morphology of the ZnO thin-film strongly depends on the density of nucleation sites that is why the $KMnO_4$ activation step has such a crucial role in the ZnO thin-films growth.[33]

The deposition mechanism of ZnO thin-films entails two different steps, as shown in Figure 4: (i) the formation of $Zn(OH)_2$ and (ii) the hydrolysis of the hydroxide. The kinetics of the zinc hydroxide formation (i) depends on the availability of its reactants; therefore, considering the alkaline pH of the bath, the limiting factor should be the availability of the cations. The hydrolysis reaction (ii) is temperature controlled, and occurs *in situ* at temperatures higher than 70°C.[45] Thus, the deposition rate is controlled by the formation of $Zn(OH)_2$ (i).

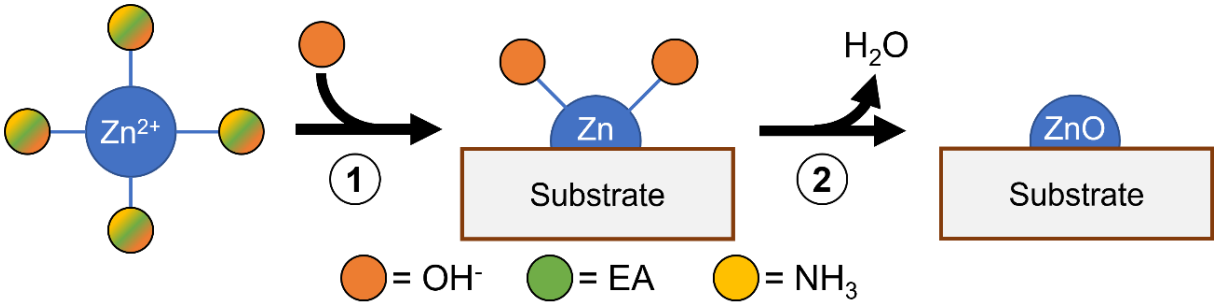


*Figure 4. Mechanism for the deposition of ZnO, starting from the complexed Zn(II) species.*

In aqueous solutions, zinc cations are solvated by water, forming aquo- and hydroxy complexes, which speciation is pH-dependent due to the amphoteric nature of Zn. Furthermore, additional complexing agents, such as ammonium derivatives and ethanolamine (EA), influence the solubility of $Zn^{2+}$ by forming $[Zn(NH_3)_n]^{2+}$, $[Zn(EA)_m]^{2+}$, $[Zn(NH_3)_n(OH)_y]^{(2-y)}$, $[Zn(EA)_m(OH)_y]^{(2-y)}$ with $n+y \leq 4$, and $m \leq 2$.[45] Therefore, the Zn available to react depends on the complexing power of the solution, which is temperature and concentration dependent. It is reported that a higher temperature decreases the complexing power, due to the instability of the Zn complexes.[46]

In addition, the hydroxide formation on the surface depends on the interactions at the solid-liquid interface. At the beginning of the deposition, the Mn(O)OH nucleation sites catalyze the growth of ZnO by the procedure already described. Nevertheless, when there is enough ZnO, the zincite structure (ZnO most stable phase) forms through an anisotropic growth.[36] Following the BFDH (Bravais, Friedel, Donnay, and Harker) model, the high index crystal planes, i.e. planes with small spacing between neighboring layers, grow faster until they grow themselves out of existence.[47,48] Figure 5 shows a scheme of the effect of differential growth rate on the zincite facets, where $k_1$ and $k_2$ are the growth kinetic constants in the 001 plane and the 011, 101, $1\bar{1}1$ planes, respectively. The BFDH model predicts that $k_2 > k$ , resulting in a flat hexagonal facet for the ZnO, although other morphologies were obtained.

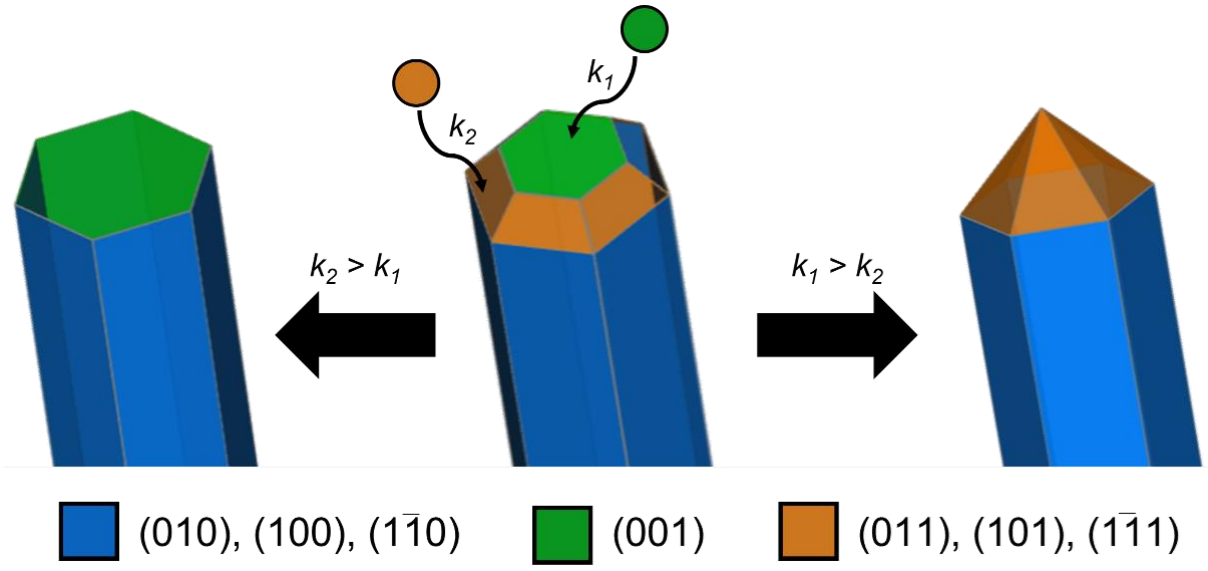


*Figure 5 Differential growth mechanism of the different facets for columnar ZnO. The facets of the ZnO crystals were indexed with WinXMorph software.*[49]

However, differential adsorption processes can occur at the interface, which modifies the surface energy of the different facets.[45] This effect changes the growth rate, and height-to-width ratio, altering the final morphology and crystallographic orientation.[47,48] Furthermore, the control of the adsorption process has been reported in the literature through structure-directing agents, which are additives that play a role in the interface and control the final morphology.[45]

Different parameters of the CBD, such as concentration of reactants and temperature, were modified to understand their effect in the final morphology, thickness, structure, and optical properties of the thin-films.

### *3.1.1. Effect of $Zn^{2+}$ concentration*

The effect of the concentration of Zn cations in solution was tested on SLG substrates activated with 0.5 mM $KMnO_4$ and 1-butanol, subjected to CBD in a growth solution with an initial concentration of 0.6 M $NH_4OH$ and 1.6 M EA at 92°C.

The increase of [$Zn^{2+}$] directly changes the availability of the metal cations in the deposition process. Figure 6a shows the different XRD patterns obtained. In all of the studied concentrations, the films adopt a preferential growth along the c-axis perpendicular to the substrate, since the most intense peak in the XRD pattern corresponds to the 002 plane (Figure 7a). However, the lowest concentration (50 mM) showed also peaks related to the (100) and (101) planes. It is worth mentioning that the reflections at 38° and 45° originate from the instrument.

In addition, the increase of Zn cation concentration decreases the crystallite size from 186.2 nm, for both 50 mM and 75 mM $Zn^{2+}$, to 59.8 nm for 100 mM $Zn^{2+}$. The latter behavior could be explained by the increase of nucleation sites, due to a decrease of the critical radius at higher $Zn^{2+}$ concentrations.[50,51] This view is consistent with the increasing coverage shown by the SEM images (Figure 6b). These images agree well also with the directionality observed in XRD (Figure 6a), where higher concentrations result in more compact columns with fewer deviations from the c-axis growth.

Figure 6c shows the transmittance as a function of the wavelength, together with the Tauc plot for the three Zn(II) concentrations. With a bandgap of 3.2 eV, the highest concentrations show similar optical behavior, while the sample of 50 mM bath presents two different bands related with its inhomogeneity. They generally show similar transparency compared with SLG up to the characteristic ZnO transition band at ~350 nm.[52] Figure 6d shows the behavior of thickness with time. In this case, the experimental data are insufficient to determine an actual growth rate. Nevertheless, in the range of times investigated, the samples prepared with $Zn^{2+}$ concentration of 100 mM showed a fast growth within 10 min, while for longer reaction times, the thickness did not change significantly, a behavior that agrees well with the reported growth for ZnO thin-films.[39]

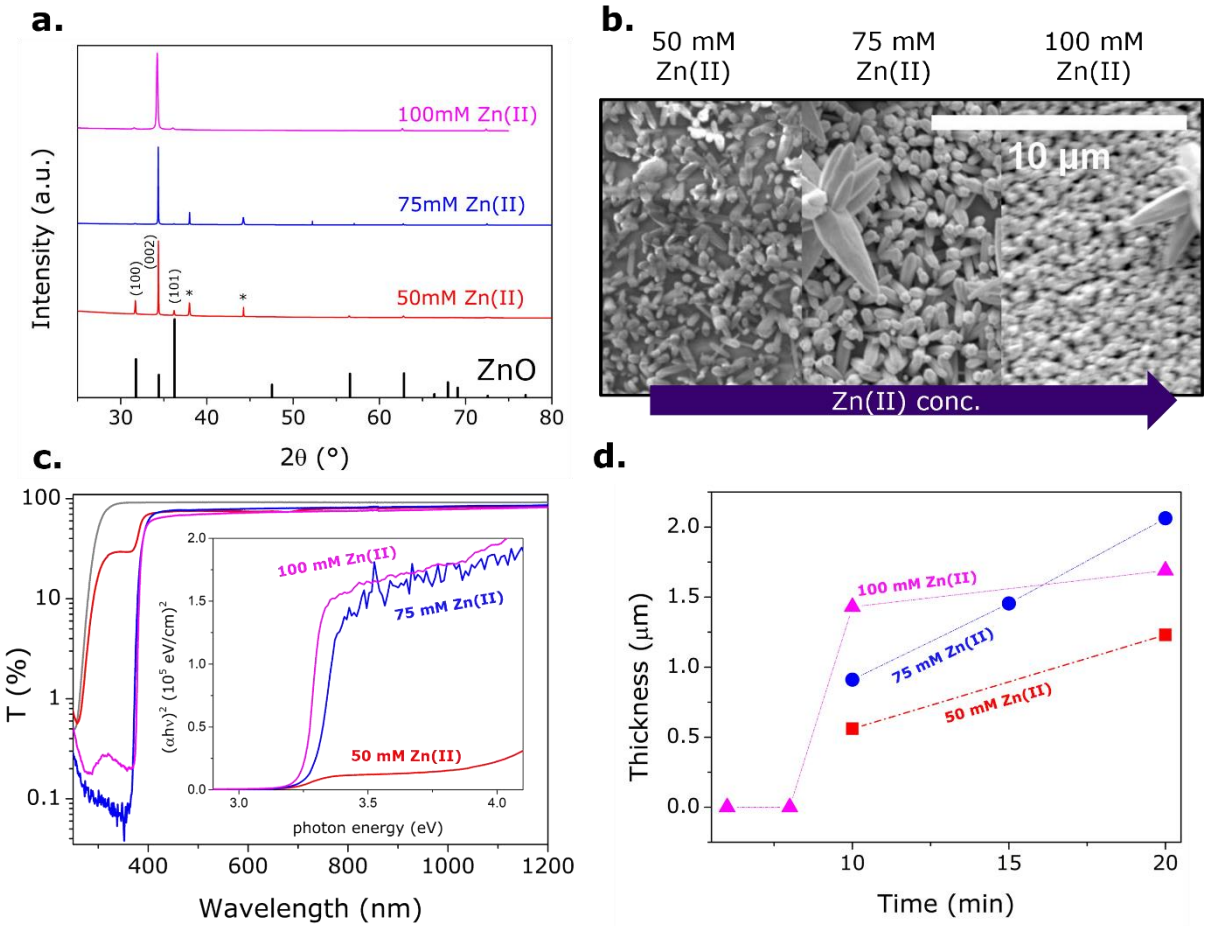


*Figure 6. (a) Rietveld refined (HighScore software) XRD patterns, (b) low magnification SEM images, (c) transmittance spectra with the respective Tauc plot as an inset, and (d) thickness as a function of time for the ZnO thin-films obtained at different $ZnSO_4$ concentrations. The peaks indicated with * are originated from the instrument.*

To sum up, the samples obtained from the 75 mM $Zn^{2+}$ bath showed the thinnest film with high (002) directionality, highest coverage, and highest homogeneity, together with the expected optical properties. Therefore, this concentration was selected for the subsequent experiments.

### *3.1.2. Effect of $KMnO_4$ concentration in the activation step*

The concentration of $KMnO_4$ during the activation step was modified to obtain SLG substrates subsequently subjected to CBD in a solution having an initial concentration of 75 mM $Zn^{2+}$, 0.6 M $NH_4OH$, 1.6 M EA at 92°C.

The increase of [$KMnO_4$] increases the nucleation sites on the SLG during the activation process, which has been reported to modify the final morphology of the film.[33]. Figure 7a shows the different patterns obtained for different activation concentrations. Here, the films display the preferential growth perpendicular to the c-axis except for the sample with 50 mM $KMnO_4$, which showed peaks related to (102), (100), (101) and (103) orientations of ZnO. The latter behavior corresponds to the one reported in the literature for high concentration of nucleation sites.[33,45]

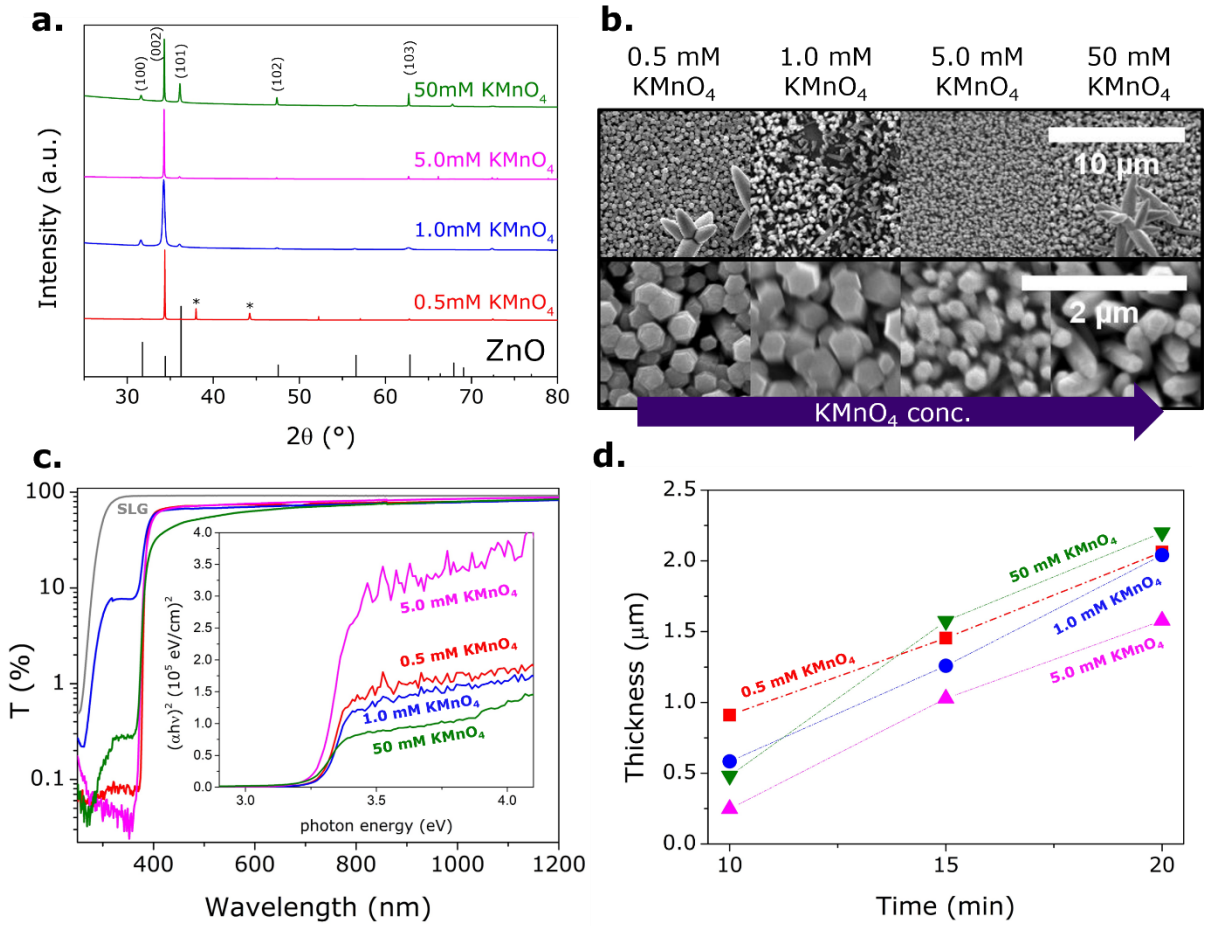


*Figure 7. (a) Rietveld refined (HighScore software) XRD patterns, (b) low and high magnification SEM images, (c) transmittance spectra with the respective Tauc plot as an inset, and (d) thickness as a function of time for the ZnO thin-films obtained at different $KMnO_4$ concentrations in the activation. The peaks indicated with * are originated from the instrument.*

In addition, the crystallite sizes were 186.2, 152.4, 140.0, and 128.8 nm for 0.5, 1.0, 5.0, and 50 mM $KMnO_4$, respectively. In this case, the crystallite size decreases with the increase in concentration of permanganate, which can be explained by the increase of nucleation sites.[50,51] Furthermore, Figure 7b shows the SEM images taken for the same samples. For the highest $KMnO_4$ activation concentration, the columns have several orientations, and the final morphology shows the presence of many orientations, as observed in the XRD pattern (Figure 7a). Moreover, in the other concentrations studied, flat-ending columns were observed with high coverage for all the samples, except for activation with 1.0 mM $KMnO_4$. It is worth mentioning that the reflections at 38 and 45° originate from the instrument.

Figure 7c contains the transmittance spectra for the samples, together with the associated Tauc plots. In this case, all the samples behave similar with the characteristic ZnO band at 350 nm

and a band gap equal to 3.2 eV, except for 1.0 mM $KMnO_4$ activated samples that show two bands, probably related to inhomogeneity. Figure 7d shows the film thickness dependence over time. For the activation concentrations below 5 mM, linear growth is observed with an average growth rate of 0.1 µm $min^{-1}$, where the starting thickness is lower with higher activation concentration. The latter effect can be explained by the increase of nucleation sites, leading to more columns having lower average height.

To summarize, the samples activated with 5.0 mM $KMnO_4$ show the thinnest films with high (002) directionality, and high coverage, together with the expected optical properties. Therefore, this concentration was selected for the subsequent experiments.

### *3.1.3. Effect of temperature*

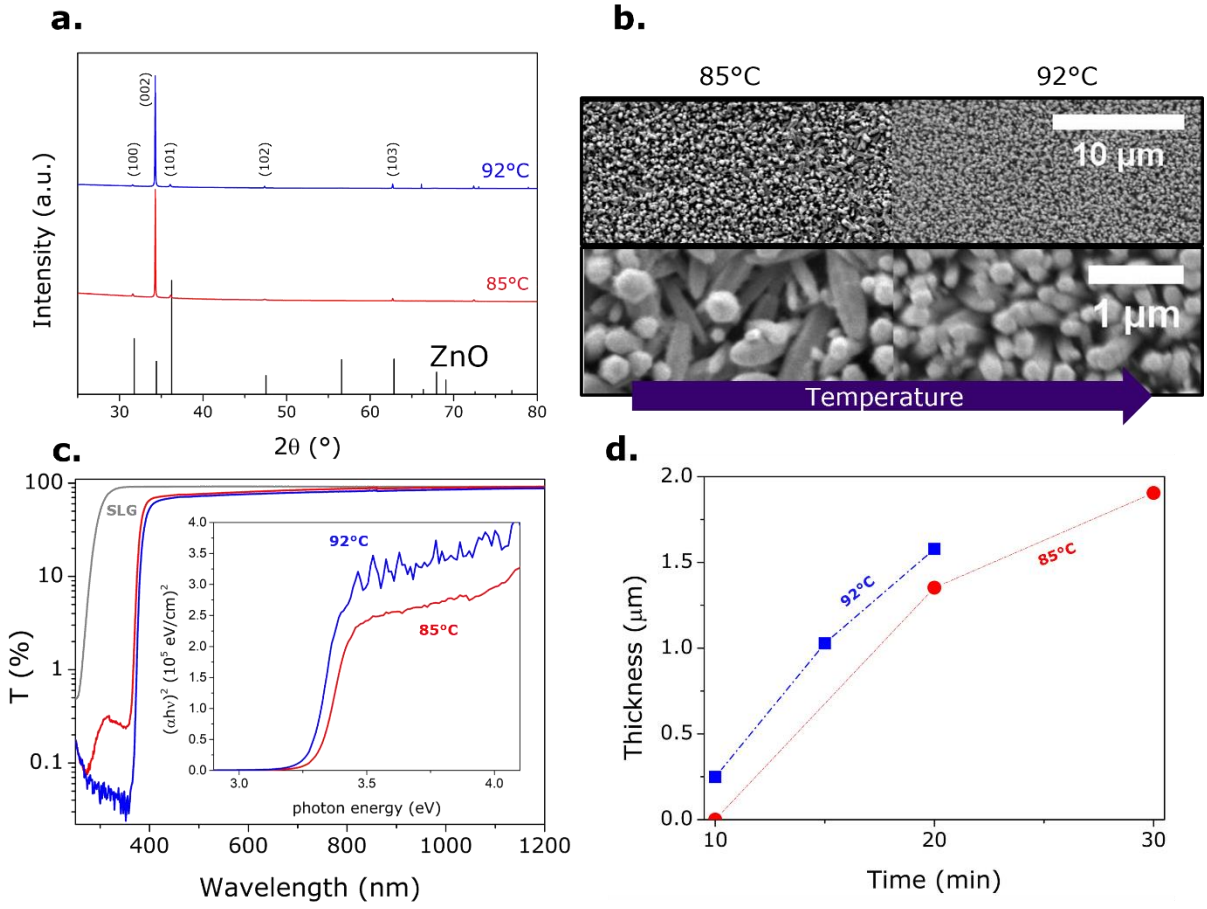


*Figure 8. (a) Rietveld refined (HighScore software) XRD patterns, (b) low and high magnification SEM images, (c) transmittance spectra with the respective Tauc plot as an inset, and (d) thickness as a function of time for the ZnO thin-films obtained at different growth temperatures.*

The effect of growth temperature was tested on SLG substrates activated with 5.0 mM $KMnO_4$ and 1-butanol, subject to CBD with a growth solution having an initial concentration of 75 mM $Zn^{2+}$, 1.6 M EA and 0.6M $NH_4OH$.

The increase in the temperature is related to faster deposition. Figure 8a shows the XRD patterns obtained for different deposition temperatures. The samples present a high orientation with the c-axis perpendicular to the substrate, as revealed by the high relative intensity of the 002 reflection. Furthermore, the crystallite sizes were 131.6 and 140 nm for 85 °C and 92 °C, respectively. The increased crystallite size is consistent with a faster kinetics at a higher

temperature. The SEM images showed more compact c-axis oriented columns for the samples grown at 92 °C (Figure 8b), with a good coverage for both deposition temperatures.

Figure 8c shows the transmittance spectra with similar behaviour for both deposition temperatures, with a unique band corresponding to the ZnO band at 350 nm and a band gap of 3.2 eV, as reported in the literature for ZnO.[53] Regarding the growth rate, Figure 8d shows the thickness for different deposition times. Here, the highest temperature gives a higher thickness and a faster growth rate by increasing the velocity of each process.

In brief the samples grown at 92°C showed a compact film with high (002) directionality, higher coverage, together with the expected optical properties. Then, this temperature was selected for the subsequent experiments.

### *3.1.4. Effect of ethanolamine concentration*

The effect of the concentration of ethanolamine was tested on SLG substrates activated with 5.0 mM $KMnO_4$ and 1-butanol, subjected to CBD in a growth solution with an initial concentration of 75 mM $Zn^{2+}$ and 0.6 M $NH_4OH$ at 92°C.

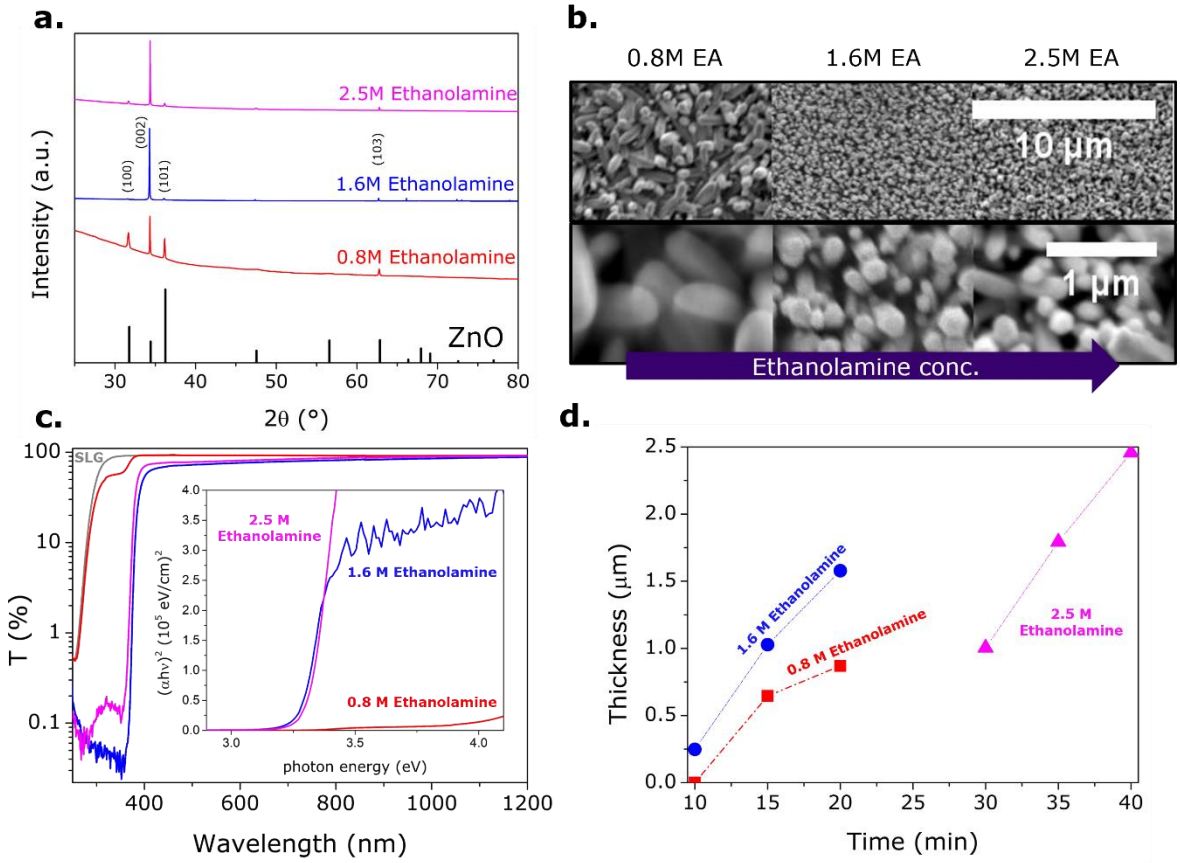


*Figure 9. (a) Rietveld refined (HighScore software) XRD patterns, (b) low and high magnification SEM images, (c) transmittance spectra with the respective Tauc plot as an inset, and (d) thickness as a function of time for the ZnO thin-films obtained at different ethanolamine (EA) concentrations.*

The increase of [EA] increases the concentration of $Zn^{2+}$-EA complexes in the deposition bath. Figure 9a shows the different patterns obtained while varying EA concentration. The lowest concentration (0.6 M EA) shows peaks related to the 100, 002, 101, and 103 planes. Furthermore, the crystallite size increases with the amount of EA in the solution, being 120.6,

140.0, 160.8 nm for 0.6, 1.6 and 2.5 M EA, respectively. The latter effect can be explained by the increase in the $Zn^{2+}$-complexes availability in the solution during the growth, therefore more Zn is supplied to ZnO nuclei, thus increasing the crystallite size.[54] Figure 9b shows the SEM images obtained. Here the lowest concentration of EA shows a layer of random-oriented conical-ending columns, with low coverage. The highest concentrations show a flat-ending columns, with similarly high coverage.

Figure 9c shows the transmittance and Tauc plot associated with these samples. The behavior observed for concentrations higher than 1.6 M was similar with a band gap around 3.2 eV, and the characteristic ZnO band. Nevertheless, the sample with the lowest EA concentration showed two bands probably caused by inhomogeneities in the film related to homogenous precipitation, which inhibits the uniform growth on the substrate. Figure 9d describes the thickness in terms of deposition time. The highest EA concentration showed visible films only after 30 min of reaction, which is probably because the system needs some time in order to reach a supersaturated condition, due to the high solubility of $Zn^{2+}$ as EA-derived complexes. Moreover, the growth for 2.5 and 1.6 M EA was linear with a rate of 0.1 μm $min^{-1}$.

In conclusion, the bath deposition with a concentration of 1.6 M EA showed the thinnest film with high (002) directionality, higher homogeneity, and coverage, together with the expected optical properties. Hence, this concentration was selected for the subsequent experiments.

### *3.1.5. Effect of $NH_4OH$ concentration*

The effect of the concentration of $NH_4OH$ was tested on SLG substrates activated with 5.0 mM $KMnO_4$ and 1-butanol, subject to CBD in a growth solution having an initial concentration of 75 mM $Zn^{2+}$ and 1.6 M EA at 92°C.

The increase of [$NH_4OH$] enhances the pH and modifies the solubility of Zn cations by the formation of hydroxy- and amino complexes. Figure 10a shows the XRD pattern obtained for different concentrations of ammonium hydroxide. For the highest pH (1.0 M $NH_4OH$), the peak of 100 plane is the most intense, which has been reported for ZnO columns growth at higher pH in hydrothermal conditions.[54] Conversely, the samples deposited in a 0.2 M $NH_4OH$ bath show a lower intensity of the XRD reflections corresponding to the (100) and (101) planes (Figure 10a). In addition, the crystallite sizes are 119.8, 140.0 and, 206.8 nm for 0.2, 0.6 and 1.0 M $NH_4OH$, respectively. This proportional increase is related to the availability of $Zn^{2+}$ complexes. SEM images (Figure 10b) confirm the features observed in XRD, with conical-ending columns for the lowest $NH_4OH$ concentration. Moreover, the highest concentration shows randomly oriented columns with a low coverage.

Figure 10c shows the transmittance spectra for the different concentrations of ammonium hydroxide. Samples deposited at bath concentrations lower than 0.6 M $NH_4OH$ reveal a similar behavior with a band gap of 3.2 eV and a unique ZnO band at 350 nm. Moreover, as mentioned before, the highest concentration shows two bands, probably related to inhomogeneities. Regarding the thickness across the deposition time (Figure 10d) the lowest concentration (0.2 M $NH_4OH$) does not show a significant change in thickness in the investigated time range, possibly due to a fast growth that reaches the steady-state equilibrium between solution cations ($Zn^{2+}_{(aq)}$) and solid (ZnO/SLG) in less than 10 min. For the highest concentration condition, the growth rate could not be estimated, and a visible film was only observed after 45min of reaction, which is probably related to the time needed to reach a supersaturated condition.

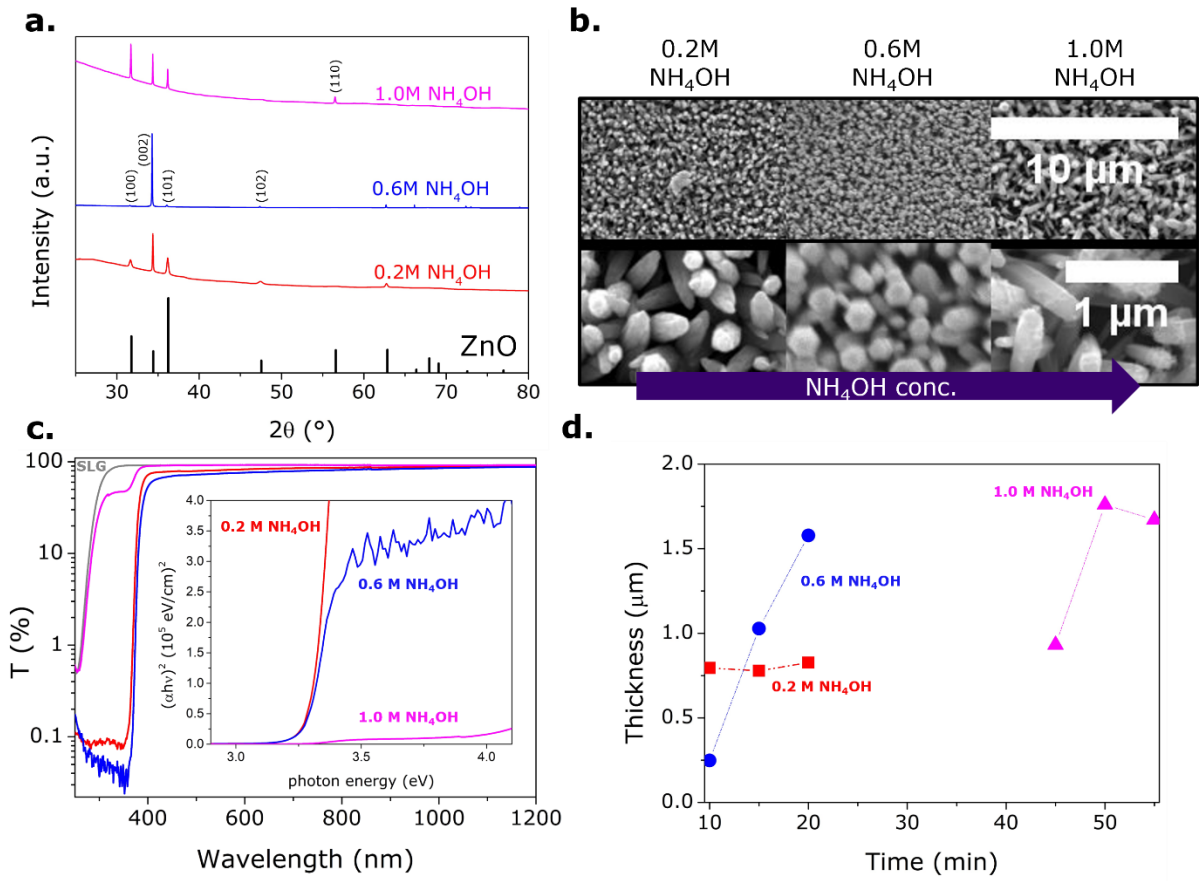


*Figure 10. (a) Rietveld refined (HighScore software) XRD patterns, (b) low and high magnification SEM images, (c) transmittance spectra with the respective Tauc plot as an inset, and (d) thickness as a function of time for the ZnO thin-films obtained at different $NH_4OH$ concentrations.*

To conclude, the bath deposition with a concentration of 0.2 M $NH_4OH$ shows the most homogeneous film with preferential (002) directionality, higher coverage, together with the expected optical properties and a low thickness that do not change significantly in the studied range. Thus, this concentration was selected for the subsequent experiments.

### 3.2. Sn-doping of ZnO thin-films onto SLG

An acidic solution of $SnCl_2$, was used to prevent the hydrolysis of Sn in DIW before the deposition.[55] Moreover, as soon as the $SnCl_2$ was added to the alkaline bath solution a precipitate was observed. Thus, the bath was mixed before the start of the deposition.

Figure 11a shows the effect of Sn concentration in the XRD patterns, being the percentage of tin defined as the [Sn]/([Sn]+[Zn]) ratio (TTZ) calculated by weight in the solution. The addition of Sn in the solution modified the peaks intensity of ZnO without introducing any additional reflection. Thus, no new phase forms up to 50% TTZ, where the peaks observed correspond to reflections of the (220) and (420) planes associated to the $ZnSn(OH)_6$ phase.[56] Moreover, with the addition of Sn the intensity of the peak related to the 002 plane decreases, until it is no longer visible for concentrations greater than 10% TTZ. The latter has been observed for metals and charged metallic complexes that differently passivate the crystal facets by electrostatic interactions.[57,58]

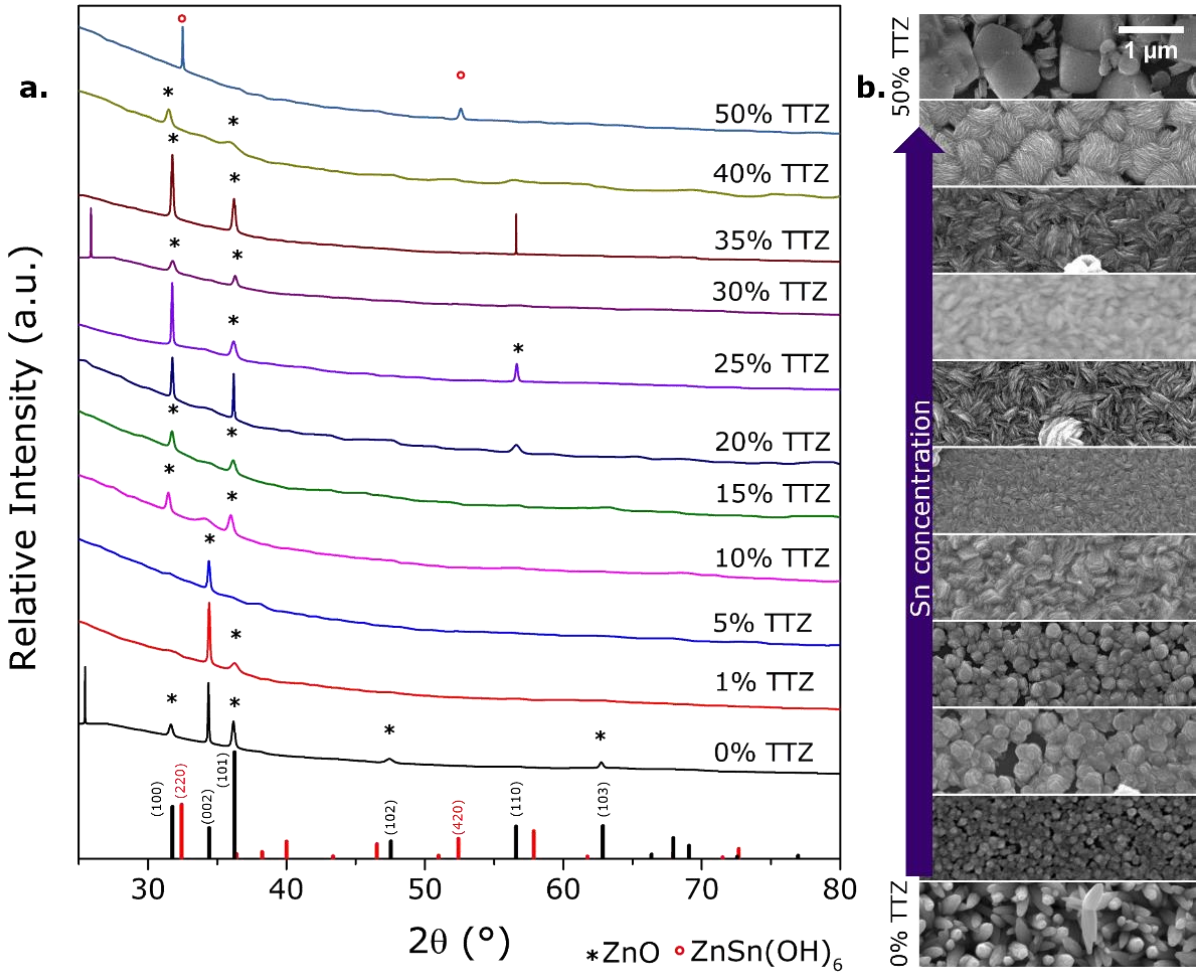


*Figure 11. (a) Rietveld refined (HighScore software) XRD patterns, (b) corresponding high magnification SEM images for the ZnO thin-films obtained at different Sn nominal doping concentrations. TTZ correspond to the [Sn]/([Sn]+[Zn]) ratio. The reference patterns at the bottom correspond to ZnO (black bars) and $ZnSn(OH)_6$ (red bars)*

The changes in crystal structure observed in the XRD patterns also have an effect on the final morphology of the film. Figure 11b shows the SEM images obtained for films grown with different concentrations of tin in the bath solution. The preferential ZnO columnar growth was not observed even for TTZ as low as 1%. In the range 1 – 10% TTZ the morphology corresponds to truncated columns with spaces without material (Figure 11b). Furthermore, the samples grown at 15% TTZ show a compact film, due to lateral growth constrained by the contact between neighboring crystals. Higher Sn concentrations give rise to compact films with elongated and small grains. Moreover, ZTO with 50% TTZ show an almost cubic morphology, in agreement with reports in the literature.[59,60] Substrates subject to 50% and higher TTZ baths show a bad coverage of the SLG, with only small regions having material, probably due to the high amount of homogenous nucleation in the bath.

All obtained ZTO films with SSZ up to 50% are rather highly transparent with transmission above 76% in the wavelength range between 500 and 1200 nm (Figure 12a). The band gap, extracted from the transmittance spectra (inset in Figure 12a), presents a non-linear increase with increasing Sn concentration, ranging between the values for ZnO and $SnO_2$, 3.2 eV and 3.9 eV respectively.[61,62] This optical behavior has been reported in ZTO films synthesized by several methods, such as spray pyrolysis, magnetron sputtering or ALD.[53,63,64] The initial band gap widening is related to the Moss-Burstein effect, i.e. the occupation of some electronic states

close to the conduction band.[64] The band gap behavior can be correlated with the changes in XRD patterns and morphology, where there were significant changes for lower SSZ films together with similar morphology in the range 20 – 40 % SSZ.

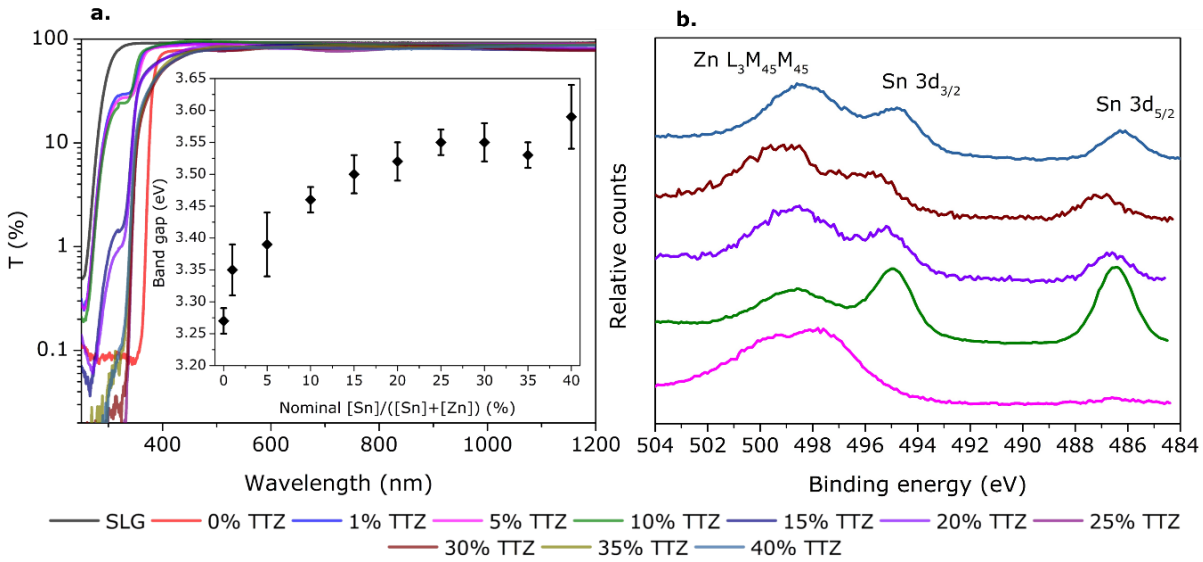


*Figure 12. (a) Transmittance spectra with the respective variation of the band gaps as a function of nominal TTZ as an inset, (b) corresponding high-resolution XPS peaks of Sn 3d for the ZTO thin-films obtained with different nominal Sn concentrations.*

Figure 12b shows the XPS spectra displaying the peaks related to the Sn $3d_{5/2}$ and Sn $3d_{3/2}$ at 486 and 495 eV, respectively for concentrations higher than 5% TTZ. The latter proves that the Sn is present in the films with a TTZ ratio in the solution higher than 5%. In addition, XPS spectra were also acquired after an *in situ* etching process and the peaks for Sn do not show a significant difference, therefore the electronic environment of the Sn cations both on the surface and inside the film is similar.

In summary, the Sn cation and its complexes modify the morphology of the final ZTO film by electrostatic interactions, together with the occupation of crystallographic sites in the ZnO wurtzite structure. In addition, an increase in the Sn concentration of the growth bath gives rise to a widening of the band gap, therefore opening the possibility of tunning the band gap from 3.2 to 3.6 eV.

### 3.3. ZTO thin-films onto other substrates

The deposition of ZTO onto other substrates was studied by dipping activated and non-activated substrates into baths with 30% TTZ. The SLG/Mo substrate does not allow the growth of ZTO thin-films neither with nor without activation, only few large particles were observed in the SEM images (Figure 13a) in the case of the activated SLG/Mo. This effect could be related to interactions between the metallic surface and ethanolamine, which inhibits the ZTO growth. The literature reported the formation of Mo(VI)-EA complexes in solution, thus ethanolamine could also interact with Mo metallic form. [65] In addition, the XRD patterns (Figure 13b) for this substrate only show peaks related to Mo.

Quartz as a substrate behaves similar to SLG, with thin-film deposition occurring only on activated substrates. Figure 13b shows the characteristic ZnO peaks for the activated quartz sample, while Figure 13a shows a compact film with lateral growth similar to that observed for

SLG. The latter was also observed for the activated CIGSe and Si wafer (Figure 13a). A possible explanation for this behavior is the presence of the same Mn(O)OH nucleation sites on the substrates. In the case of the Si-wafer a film was observed in both cases (activated and non-activated) with different morphologies, being compact and elongated grains for the non-activated Si wafer, as it was observed for SLG at higher TTZ. ZTO thin-films grow on CIGSe also without activation; the films display truncated columns, as observed for SLG at lower TTZ. In addition, the XRD patterns in Figure 13b show the peaks related to ZnO and the characteristic ones of each substrate.

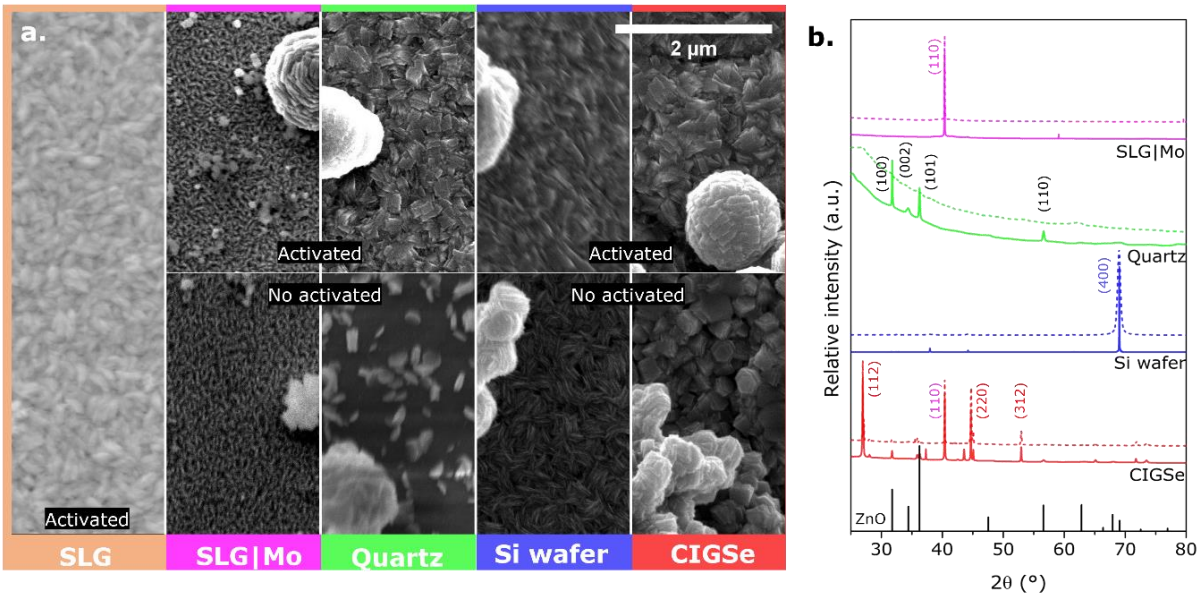


*Figure 13. (a) High-magnification SEM images and (b) Rietveld refined (HighScore software) XRD patterns for activated (solid lines) and non-activated (dashed lines) substrates subjected to CBD with a composition of 30% SSZ.*

Therefore, in a bath with the same TTZ, the Si wafer favors films with elongated and compact grains, while CIGSe promotes columnar growth that is at the same time inhibited by the Sn cations giving rise to truncated columns.

### 3.4. ZTO thin-films as buffer layers for thin-film solar cells

By knowing that the deposition of ZTO onto CIGSe was possible without the activation step, as shown in Figure 13, several ZTO-coated CIGSe samples were fabricated.

As observed in the SLG substrates, the change in Sn nominal concentration produce different morphologies in the thin-films. Figure 14 shows a cross-section and top-view SEM images of ZTO thin-films on CIGSe for different TTZ. The ZTO thin-film shows a different morphology from the CIGSe substrate (Figure 14b) with smaller grains. For 10% TTZ a truncated columns morphology is observed (Figure 14d), while 20% TTZ yields a morphology with small, elongated grains (Figure 14f). In the case of 30% TTZ, the grains assume a spherical shape (Figure 14h), while for the highest concentration tested the spheres become round cuboids (Figure 14j). In addition, with a deposition time of 30 min a thickness of 350±15 nm was obtained for all the concentrations studied.

The samples were analyzed with XPS to confirm the electronic state and composition. The survey shows the presence of Zn and O (Figure 15a) for all the studied TTZ compositions. Figure 15b, and c show the peaks related to O 1s on the thin-film surface and interior, i.e. before

and after etching with an Ar beam for 90s. Regarding the samples with 10 and 20% TTZ the peak at 531 eV is related to the $O^{2-}$ position in the wurtzite structure, while the peak at 530 eV corresponds to oxygen vacancies before and after etching.[66,67] Furthermore, for concentrations higher than 30%, TTZ at the surface and inside of the film present differences. At the surface the peak related to oxygen vacancies is the only one observed. While, after the etching the peak at low energy related to the wurtzite structure is also present. In general, the intensity of the peak corresponding to the $O^{2-}$ position in the crystal structure is increased after the etching process.

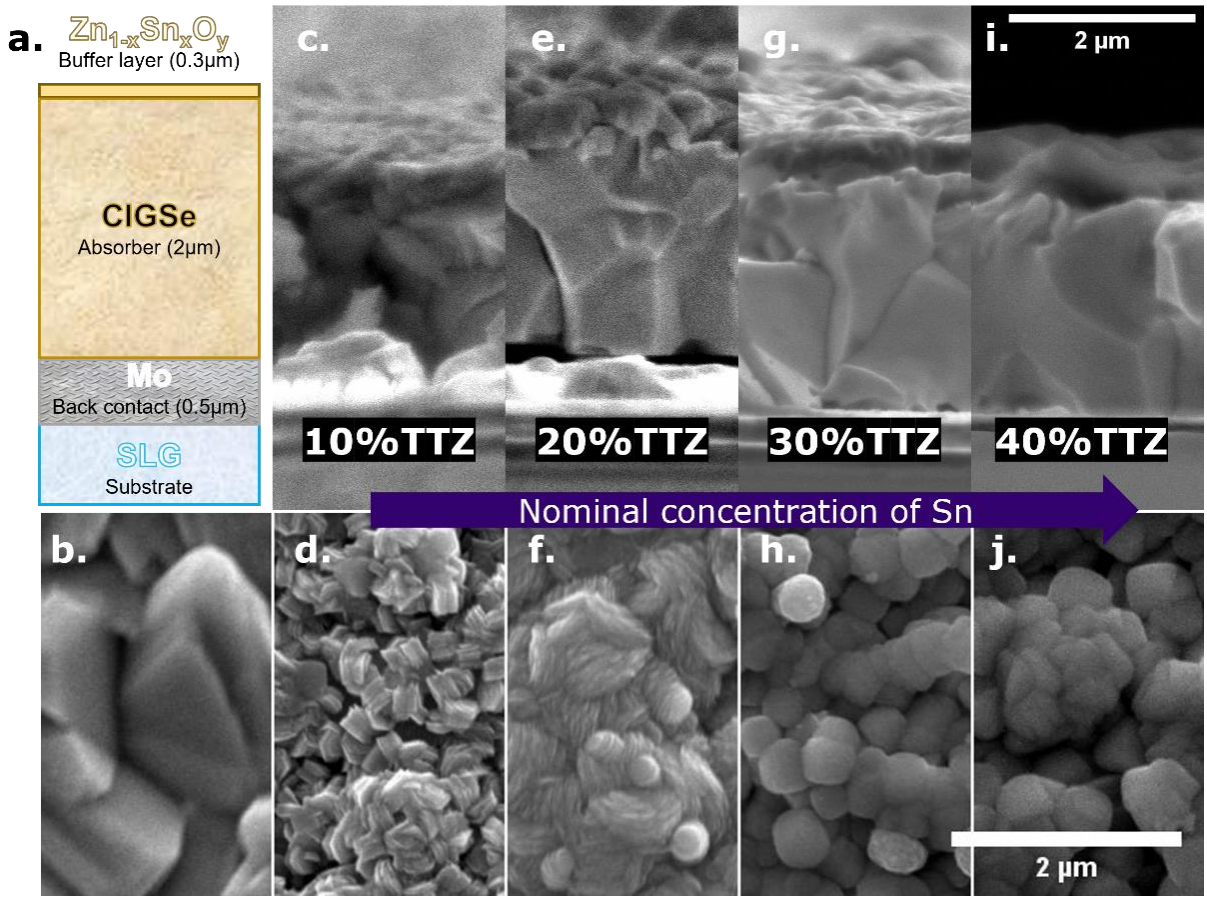


*Figure 14. (a) Scheme showing the CIGSe used as a substrate for the deposition of the ZTO thin-films. Cross-section and top view SEM images of ZTO thin-films grown onto CIGSe with (c, d) 10% TTZ, (e, f) 20% TTZ, (g, h) 30% TTZ, (i, j) 40% TTZ. (b) Top view of CIGSe.*

Figure 15d shows the peaks related to the spin-orbit coupling of Zn $2p_{3/2}$ and Zn $2p_{1/2}$ at 1021 and 1044 eV, respectively. The latter indicates a normal $Zn^{2+}$ state.[66] Figure 15e shows the peaks corresponding to the spin-orbit coupling of Sn $3d_{5/2}$ and Sn $3d_{3/2}$ at 486 and 495 eV, respectively. In addition, Figure 15e shows a peak corresponding to the Auger Zn $L_3M_{45}M_{45}$ transition at 498 – 499 eV that overlaps with the peak of Sn $3d_{3/2}$, the intensity of this signal decreases with increasing of TTZ content. Furthermore, this peak shifts to higher energy when the Sn concentration is higher than or equal to 30% TTZ. It is reported that the probability of this kind of transitions is highly related to the morphology, which drastically changes after 30% TTZ.[66,68] Nevertheless, the peaks were not enough to clearly determine the electronic state of the Sn cations, because these electronic states differ more in the position of the valence band.[69] Therefore, further studies are needed to determine the electronic state of the Sn cations.

The composition of the film was also studied by XPS, and an increase with the Sn content in solution was related to a TTZ increase in the film both on the surface and inside (Figure 15f). Nevertheless, the increase was not linear with a maximum of 28% TTZ for 40% TTZ in solution. Therefore, the difference between the solution and the thin-film TTZ could be related to the homogenous nucleation observed as precipitation during the deposition. Moreover, the relationship between the solution and thin-film TTZ must be further studied.

Figure 16 shows the solar cell parameters obtained for CdS-based and ZTO-based devices with different TTZ. The CdS-based solar cells show a sharp distribution for the PCE with an average of 5.8±0.5 %, and a $J_{sc}$ and $V_{oc}$ of 24.0±0.9 mA $cm^{-2}$ and 0.446±0.005 V, respectively. The ZTO-based solar cells show a wide distribution of PCE (Figure 16a), achieving the best efficiency for the 20% TTZ sample (9±3%) and a champion cell showing 11% efficiency. This improved performance is due to a greater FF, $J_{sc}$ and $V_{oc}$, with averages of 58±19 %, 28±7 mA $cm^{-2}$ and 0.5±0.1 V, respectively. The significant increase of open-circuit voltage is related to the increase in band gap of the ZTO buffer layer, which allows an improvement in conduction band offset that reduces the interface recombination.[31]

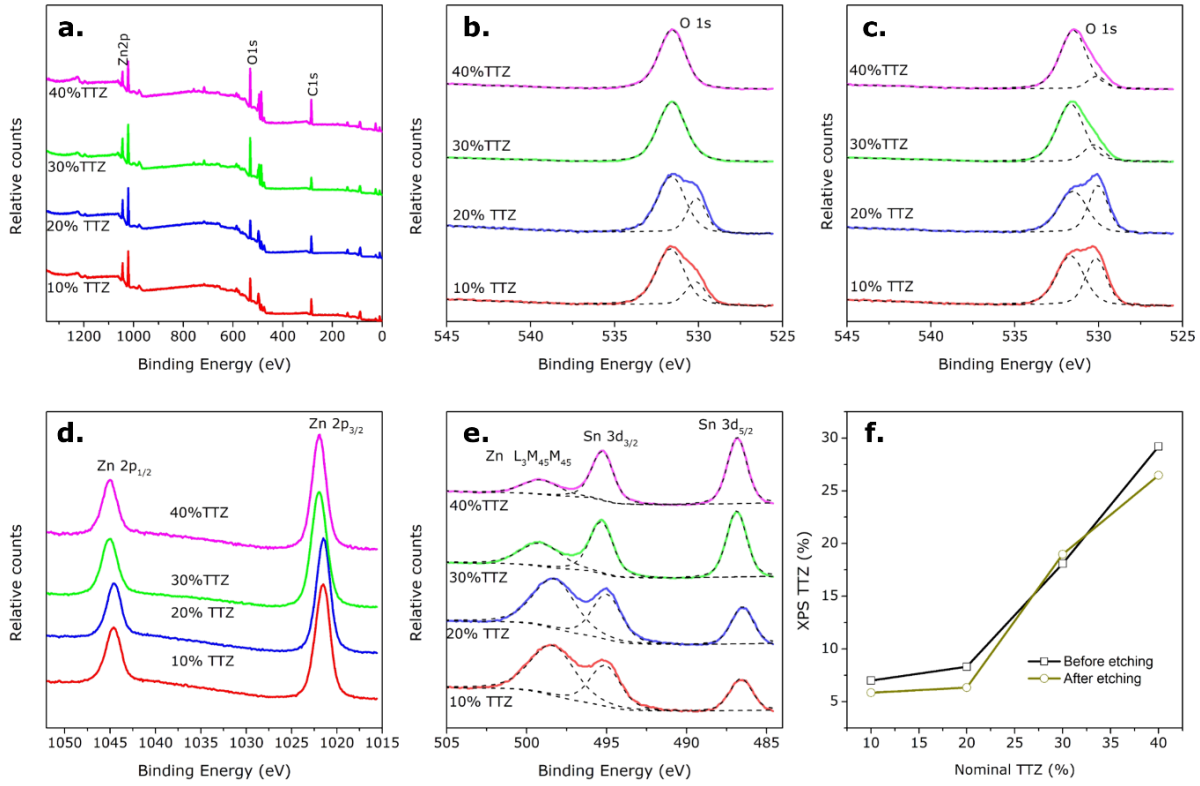


*Figure 15. (a) Survey XPS spectra, (b, c) and high-resolution XPS peaks of O 1s, (d) Zn 2p, (e) and Sn 3d. The peaks of O 1s correspond to the signal (b) before an etching for 90s in an Ar atmosphere and (c) after. The dashed lines show the fitting. (f) XPS TTZ as a function of nominal TTZ in the bath solution at the surface and after the etching of 90s.*

ZTO-based solar cells up to 30% TTZ show a higher FF than CdS-based solar cells, which is related to lower $R_{series}$ and higher $R_{shunt}$, therefore a higher or similar PCE is observed. The performance of the 40% TTZ solar cell was worse than the reference CdS. Thus, according to the XPS results, the optimal Sn concentration range is close to 20% TTZ in solution, leading to an 8% TTZ in the ZTO film. It is worth mentioning that there is a significant difference in the performance of the 10% TTZ and 20% TTZ ZTO-based solar cells, even though these two buffer layers differ only by 1% absolute in the measured Sn composition. Therefore, the Sn

concentration in this range is a critical parameter for the final performance of the device. It is worth to mention that further investigation must be done to understand the concentration of Sn at the CIGSe/ZTO interface, which is the region that determines the actual CBO.

ZTO-based solar cells perform better than its CdS counterpart even with a buffer layer six times thicker, which gives room for improvement in terms of performance since it has been reported that thinner ZTO buffer layers result in higher efficiencies.[27] In addition, the higher thickness can be related to lower transparency, negatively impacting the short circuit current density. Figure 16 also shows a wider distribution for all the parameters in the ZTO-based solar cells, which could be related to inhomogeneities present in the p-n junction, possibly resulting from inhomogeneities in the unstirred bath, where the deposition is performed.

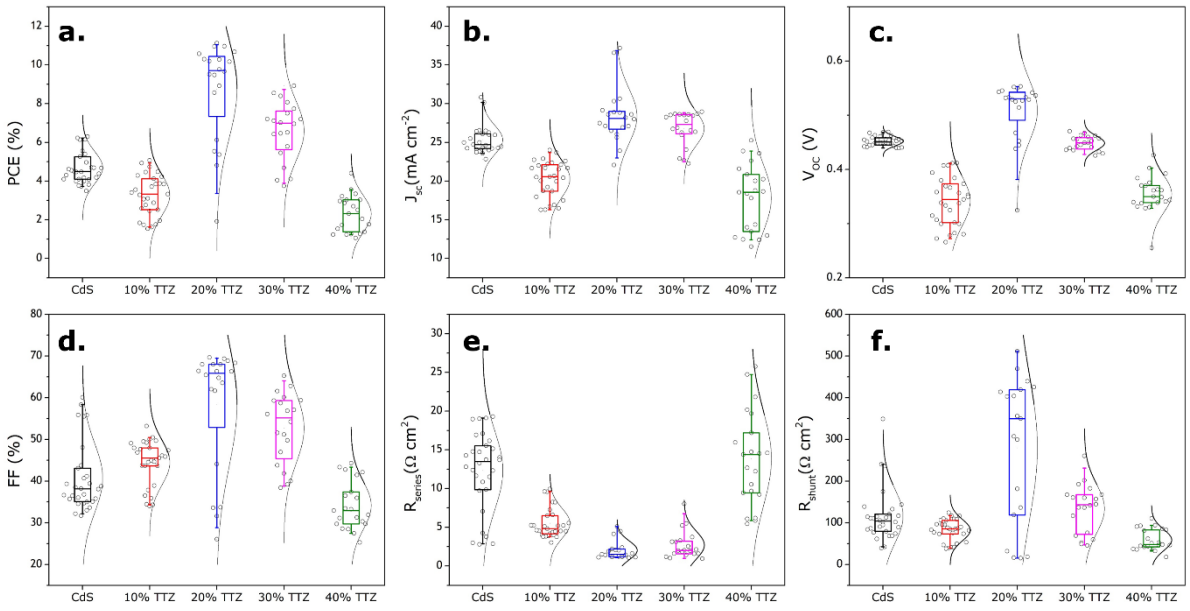


*Figure 16. Comparison of the cell performances for CdS-based SC and ZTO-based solar cells with different compositions for the ZTO buffer layers. (a) power conversion efficiency, (b) short circuit current density, (c) open circuit voltage, (d) fill factor, (e) series resistance, (f) shunt resistance*

Figure 17 shows the champion cells' JV curves under light and in dark conditions, together with the respective EQE spectra. The area under these spectra should correspond to the measured value of short-circuit current in the JV curves. However, this accordance was not observed, which is attributed to poor electric contacts established with the contact tips in this setup. Thus, further experiments with an optimized EQE setup should be done in the future. Nevertheless, the spectrum shape is considered reliable.

The increase in the blue range (short wavelength) is related with the band gap of the buffer layer (*31*), and Figure 17b shows that up to 30% TTZ the curve slope in the blue range is increasing proportionally to TTZ. The highest Sn concentration has a slope similar to the 30% TTZ, probably because the change of band gap is not significant in this range of concentrations (section 3.2). In addition, the CdS device starts losing efficiency at a shorter wavelength than the ZTO devices. Besides, the shape in the range 500 – 800 nm is significantly different for the ZTO and CdS devices. ZTO samples present a constant increase, while CdS cells indicates an abrupt increase followed by a constant quantum efficiency.

Furthermore, the results for the 20% TTZ ZTO-based samples show that the high PCE is more related to the significantly greater $V_{oc}$, together with a small $R_{series}$ and a high $R_{shunt}$, which results in a greater FF. Thus, optimizing of the thickness of the sample to obtain a higher transparency, and therefore a higher current should result in an even higher performance. In addition, the EQE spectra for the 10 and 40% TTZ solar cells (7 and 28% XPS TTZ) show a low EQE.

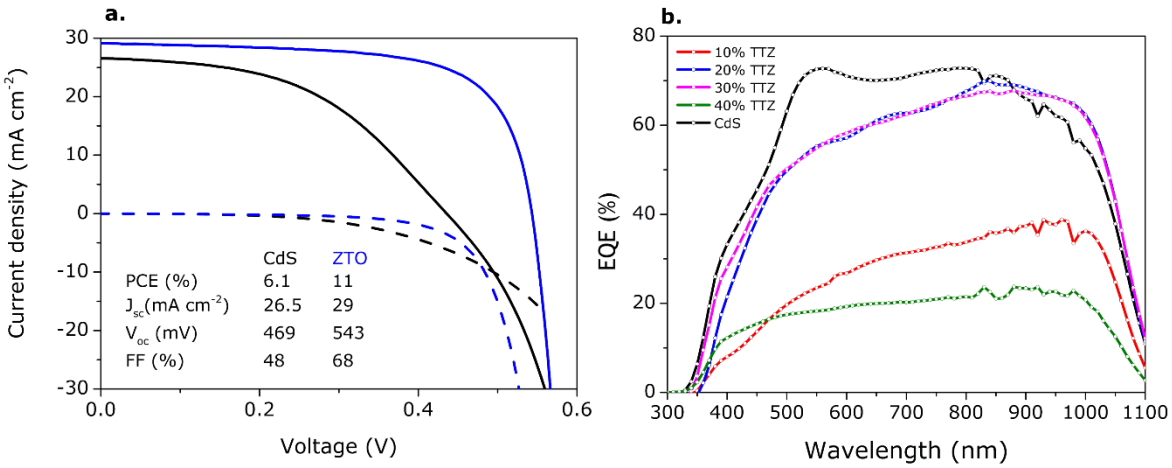


*Figure 17. (a) JV curves under illumination (solid line) and in dark conditions (dashed line) or CIGSe solar cells with CdS (black) and 20% TTZ ZTO (blue) buffer layer, with the solar cell parameters, together with the corresponding (b) EQE spectra for the champion cells of the CdS- and ZTO-based solar cells.*

In conclusion, ZTO thin-films show an opportunity to obtain Cd-free CIGSe solar cells with comparable (and in this instance even greater) PCE. Nevertheless, there is still room for optimization regarding Sn content and thickness of the ZTO thin-films.

## 4. Conclusions

ZnO thin-films were obtained on activated SLG by CBD. In this process, the effect of different parameters was studied. For example, the increase of Zn(II) concentration results in thicker films with high (002) directionality. The increase of $KMnO_4$ in the activation process creates more nucleation sites for the ZnO growth, which leads to a higher coverage. A higher deposition temperature also improved the coverage. In addition, a thinner film with high coverage was obtained by decreasing the concentration of $NH_4OH$.

The introduction of the Sn cations and their respective complexes in the CBD solution affects the final morphology by electrostatic interactions in the deposition process and the occupation of crystallographic sites in the ZnO wurtzite structure. The latter also allows the band gap modification, thus opening the possibility to tune the band gap from 3.2 to 3.6 eV.

ZTO thin-films grown onto different activated substrates (SLG, CIGSe, Si wafer, Quartz) do not present significant differences in terms of morphology due to the presence of the same Mn(O)OH nucleation sites on the substrates. Nevertheless, for the same Sn content, the Si wafer favors films with elongated and compact grains, while CIGSe promotes columnar growth that is simultaneously inhibited by the Sn cations giving rise to truncated columns. Moreover, ZTO thin-films do not appear to grow on Mo/SLG even in the presence of activation.

ZTO-based solar cells prepared with a TTZ composition of 20% in solution (8% TTZ in the film measured by XPS) show a maximum efficiency of 11%, which is 5% absolute greater than the Cd-based reference. This efficiency increase is related to a higher $V_{oc}$, with a greater FF due to lower $R_{series}$ and higher $R_{shunt}$. Nevertheless, there is still room for optimization regarding the homogeneity and thickness of the ZTO thin-films. Likewise, further investigation is required in CBO optimization, tuning band gap and composition of the buffer layer.

**Acknowledgments**

I acknowledge the support of the Erasmus+: Erasmus Mundus program of the European Union. In addition, I would like to extend my deepest gratitude to my supervisors, Sascha Sadewasser, in Portugal and, Diego Colombara, in Italy, together with Christian Rossi, who made this work possible. Many thanks to Marina Alves, Pedro Santos, Ishwor Khatri, and my other colleagues at INL. Finally, I also want to thank my family (Martha, Luisa, Jonathan, Jorge, Gerardo), friends (Eva, Simão, Teodor, Yutzil, Marta, Alicja, Ola, Andrea, Lorenzo, Christian, Fran, Basia), and teachers for being always there for me.

**References**

1. United Nations. Energy - United Nations Sustainable Development. https://www.un.org/sustainabledevelopment/energy/.
2. European Commission. Cluster 5: Climate, Energy and Mobility. *European Commission - European Commission* https://ec.europa.eu/info/research-and-innovation/funding/funding-opportunities/funding-programmes-and-open-calls/horizon-europe/cluster-5-climate-energy-and-mobility_en.
3. FCT. Agendas Temáticas: Sistemas Sustentáveis de Energia. https://www.fct.pt/agendastematicas/sissusenerg.phtml.pt.
4. Minciencias. Plan de convocatorias ASCTeI 2021-2022. *Minciencias* https://minciencias.gov.co/convocatorias-asctei.
5. Hannah Ritchie, M. R. & Rosado, P. Energy. *Our World in Data* (2020).
6. Ehrlich, R. & Geller, H. *Renewable energy: a first course*. (CRC Press, Taylor & Francis Group, 2018).
7. Lee, Y., Park, C., Balaji, N., Lee, Y.-J. & Dao, V. A. High-efficiency Silicon Solar Cells: A Review. *Isr. J. Chem.* **55**, 1050–1063 (2015).
8. Lee, T. D. & Ebong, A. U. A review of thin film solar cell technologies and challenges. *Renewable and Sustainable Energy Reviews* **70**, 1286–1297 (2017).
9. Aamir Iqbal, M. *et al.* Materials for Photovoltaics: Overview, Generations, Recent Advancements and Future Prospects. in *Thin Films Photovoltaics* (eds. Zaidi, B. & Shekhar, C.) (IntechOpen, 2022). doi:10.5772/intechopen.101449.
10. Mirabi, E., Akrami Abarghuie, F. & Arazi, R. Integration of buildings with third-generation photovoltaic solar cells: a review. *Clean Energy* **5**, 505–526 (2021).
11. Buitrago, E., Novello, A. M. & Meyer, T. Third-Generation Solar Cells: Toxicity and Risk of Exposure. *HCA* **103**, (2020).
12. Ramanujam, J. *et al.* Flexible CIGS, CdTe and a-Si:H based thin film solar cells: A review. *Progress in Materials Science* **110**, 100619 (2020).
13. Ashok, A. *et al.* Characterizations of a Selenized Cu(In1-xGax)Se2 Thin Film Absorber Layer Fabricated By a Three-Stage Hybrid Method. in *2018 15th International Conference on Electrical Engineering, Computing Science and Automatic Control (CCE)* 1–6 (IEEE, 2018). doi:10.1109/ICEEE.2018.8533902.

14. Nakamura, M. *et al.* Cd-Free Cu(In,Ga)(Se,S) $_2$ Thin-Film Solar Cell With Record Efficiency of 23.35%. *IEEE J. Photovoltaics* **9**, 1863–1867 (2019).
15. National Renewable Energy Laboratory. Best Research-Cell Efficiency Chart. https://www.nrel.gov/pv/cell-efficiency.html.
16. *Renewable energy: power for a sustainable future*. (Oxford University Press in association with the Open University, 1996).
17. Honsberg, C. B. & Bowden, S. G. Photovoltaics Education Website. https://www.pveducation.org/ (2019).
18. Hirst, L. C. & Ekins-Daukes, N. J. Fundamental losses in solar cells. *Prog. Photovolt: Res. Appl.* **19**, 286–293 (2011).
19. Aftabuzzaman, M., Sarker, S., Lu, C. & Kim, H. K. In-depth understanding of the energy loss and efficiency limit of dye-sensitized solar cells under outdoor and indoor conditions. *J. Mater. Chem. A* **9**, 24830–24848 (2021).
20. Hall, R. N. Electron-Hole Recombination in Germanium. *Phys. Rev.* **87**, 387–387 (1952).
21. Shockley, W. & Read, W. T. Statistics of the Recombinations of Holes and Electrons. *Phys. Rev.* **87**, 835–842 (1952).
22. Salomé, P. M. P. *et al.* CdS and Zn1−xSnxOy buffer layers for CIGS solar cells. *Solar Energy Materials and Solar Cells* **159**, 272–281 (2017).
23. Lindahl, J. *et al.* Deposition temperature induced conduction band changes in zinc tin oxide buffer layers for Cu(In,Ga)Se2 solar cells. *Solar Energy Materials and Solar Cells* **144**, 684–690 (2016).
24. Rasouli, F. & Madani, M. R. Analysis of CIGS-based thin film tandem solar cell with ZnS buffer layers. *Opt Quant Electron* **52**, 481 (2020).
25. Fuster, D. *et al.* System for manufacturing complete Cu(In,Ga)Se2 solar cells in situ under vacuum. *Solar Energy* **198**, 490–498 (2020).
26. Park, G. S. *et al.* Achieving 14.4% Alcohol-Based Solution-Processed Cu(In,Ga)(S,Se) $_2$ Thin Film Solar Cell through Interface Engineering. *ACS Appl. Mater. Interfaces* **10**, 9894–9899 (2018).
27. Lindahl, J. *et al.* The effect of Zn $_{1-x}$ Sn $_x$ O $_y$ buffer layer thickness in 18.0% efficient Cd-free Cu(In,Ga)Se $_2$ solar cells: Effect of Zn $_{1-x}$ Sn $_x$ O $_y$ buffer layer thickness in CIGS solar cells. *Prog. Photovolt: Res. Appl.* **21**, 1588–1597 (2013).
28. Doña, J. M. & Herrero, J. Dependence of Electro-optical Properties on the Deposition Conditions of Chemical Bath Deposited CdS Thin Films. *J. Electrochem. Soc.* **144**, 4091–4098 (1997).
29. Haider, F. U. *et al.* Cadmium toxicity in plants: Impacts and remediation strategies. *Ecotoxicology and Environmental Safety* **211**, 111887 (2021).
30. Tokumoto, M., Lee, J.-Y. & Satoh, M. Transcription Factors and Downstream Genes in Cadmium Toxicity. *Biological & Pharmaceutical Bulletin* **42**, 1083–1088 (2019).
31. Larsson, F. *et al.* Record 1.0 V open-circuit voltage in wide band gap chalcopyrite solar cells. *Prog. Photovolt: Res. Appl.* **25**, 755–763 (2017).
32. Hashimoto, Y., Kohara, N., Negami, T., Nishitani, N. & Wada, T. Chemical bath deposition of Cds buffer layer for GIGS solar cells. *Solar Energy Materials and Solar Cells* **50**, 71–77 (1998).
33. Kokotov, M. & Hodes, G. Reliable chemical bath deposition of ZnO films with controllable morphology from ethanolamine-based solutions using KMnO4 substrate activation. *J. Mater. Chem.* **19**, 3847 (2009).
34. Taunk, P. B., Das, R., Bisen, D. P., Tamrakar, R. K. & Rathor, N. Synthesis and optical properties of chemical bath deposited ZnO thin film. *Karbala International Journal of Modern Science* **1**, 159–165 (2015).

35. Guire, M. R. D., Bauermann, L. P., Parikh, H. & Bill, J. Chemical Bath Deposition. in *Chemical Solution Deposition of Functional Oxide Thin Films* (eds. Schneller, T., Waser, R., Kosec, M. & Payne, D.) 319–339 (Springer Vienna, 2013). doi:10.1007/978-3-211-99311-8_14.
36. Govender, K., Boyle, D. S., Kenway, P. B. & O'Brien, P. Understanding the factors that govern the deposition and morphology of thin films of ZnO from aqueous solution. *J. Mater. Chem.* **14**, 2575–2591 (2004).
37. Baviskar, P. K., Nikam, P. R., Gargote, S. S., Ennaoui, A. & Sankapal, B. R. Controlled synthesis of ZnO nanostructures with assorted morphologies via simple solution chemistry. *Journal of Alloys and Compounds* **551**, 233–242 (2013).
38. Edinger, S. *et al.* Comparison of chemical bath-deposited ZnO films doped with Al, Ga and In. *J Mater Sci* **52**, 9410–9423 (2017).
39. Lehmann, J. *et al.* Reliable wet-chemical cleaning of natively oxidized high-efficiency Cu(In,Ga)Se $_2$ thin-film solar cell absorbers. *Journal of Applied Physics* **116**, 233502 (2014).
40. Colombara, D. *et al.* Chemical instability at chalcogenide surfaces impacts chalcopyrite devices well beyond the surface. *Nat Commun* **11**, 3634 (2020).
41. Salvador, Paulo Miguel Babo Cunha. Deposition and characterization of CdS and ZnO:Al thin films for Cu(In,Ga)Se solar cells. (Universidade do Minho, 2017).
42. Tauc, J. Optical properties and electronic structure of amorphous Ge and Si. *Materials Research Bulletin* **3**, 37–46 (1968).
43. Rietveld, H. M. A profile refinement method for nuclear and magnetic structures. *J Appl Crystallogr* **2**, 65–71 (1969).
44. Scherrer, P. Bestimmung der inneren Struktur und der Größe von Kolloidteilchen mittels Röntgenstrahlen. in *Kolloidchemie Ein Lehrbuch* 387–409 (Springer Berlin Heidelberg, 1912). doi:10.1007/978-3-662-33915-2_7.
45. Peter, F. Chemical bath deposition of transparent conductive zinc oxide thin films for solar cell applications. 119 p. (ETH Zurich, 2017). doi:10.3929/ETHZ-A-010874054.
46. Wang, X. *et al.* Controllable ZnO Architectures by Ethanolamine-Assisted Hydrothermal Reaction for Enhanced Photocatalytic Activity. *J. Phys. Chem. C* **115**, 2769–2775 (2011).
47. Goel, S., Sinha, N., Yadav, H. & Kumar, B. On the prediction of external shape of ZnO nanocrystals. *Physica E: Low-dimensional Systems and Nanostructures* **106**, 291–297 (2019).
48. Baxter, J. B., Wu, F. & Aydil, E. S. Growth mechanism and characterization of zinc oxide hexagonal columns. *Appl. Phys. Lett.* **83**, 3797–3799 (2003).
49. Kaminsky, W. *WinXMorph* : a computer program to draw crystal morphology, growth sectors and cross sections with export files in VRML V2.0 utf8-virtual reality format. *J Appl Crystallogr* **38**, 566–567 (2005).
50. Pal, M., Pal, U., Jiménez, J. M. G. Y. & Pérez-Rodríguez, F. Effects of crystallization and dopant concentration on the emission behavior of TiO2:Eu nanophosphors. *Nanoscale Res Lett* **7**, 1 (2012).
51. Sharifi Dehsari, H. *et al.* Effect of precursor concentration on size evolution of iron oxide nanoparticles. *CrystEngComm* **19**, 6694–6702 (2017).
52. Berumen-Torres, J. A. *et al.* Low resistivity annealed tin-doped zinc oxide thin films prepared by the sol gel technique. *Materials Science and Engineering: B* **268**, 115134 (2021).
53. Wahila, M. J. *et al.* Accelerated optimization of transparent, amorphous zinc-tin-oxide thin films for optoelectronic applications. *APL Materials* **7**, 022509 (2019).
54. Lu, C.-H. & Yeh, C.-H. Influence of hydrothermal conditions on the morphology and particle size of zinc oxide powder. *Ceramics International* **26**, 351–357 (2000).

55. Pettine, M., Millero, F. J. & Macchi, G. Hydrolysis of tin(II) in aqueous solutions. *Anal. Chem.* **53**, 1039–1043 (1981).
56. Wang, X. *et al.* Structural inheritance and change from ZnSn(OH)6 to ZnSnO3 compounds used for ethanol sensors: Effects of oxygen vacancies, temperature and UV on gas-sensing properties. *Journal of Alloys and Compounds* **829**, 154445 (2020).
57. Joo, J., Chow, B. Y., Prakash, M., Boyden, E. S. & Jacobson, J. M. Face-selective electrostatic control of hydrothermal zinc oxide nanowire synthesis. *Nature Mater* **10**, 596–601 (2011).
58. Peiró, A. M., Ayllón, J. A., Peral, J., Domènech, X. & Domingo, C. Microwave activated chemical bath deposition (MW-CBD) of zinc oxide: Influence of bath composition and substrate characteristics. *Journal of Crystal Growth* **285**, 6–16 (2005).
59. Fu, X. *et al.* Hydroxide ZnSn(OH)6: A promising new photocatalyst for benzene degradation. *Applied Catalysis B: Environmental* **91**, 67–72 (2009).
60. He, Q. *et al.* Controlled growth and thermal decomposition of well-dispersed and uniform ZnSn(OH)6 submicrocubes. *Journal of Alloys and Compounds* **607**, 193–197 (2014).
61. Zhou, W., Liu, Y., Yang, Y. & Wu, P. Band Gap Engineering of $SnO_2$ by Epitaxial Strain: Experimental and Theoretical Investigations. *J. Phys. Chem. C* **118**, 6448–6453 (2014).
62. Al-Gaashani, R., Radiman, S., Tabet, N. & Daud, A. R. Optical properties of SnO2 nanostructures prepared via one-step thermal decomposition of tin (II) chloride dihydrate. *Materials Science and Engineering: B* **177**, 462–470 (2012).
63. Mullings, M. N. *et al.* Thin film characterization of zinc tin oxide deposited by thermal atomic layer deposition. *Thin Solid Films* **556**, 186–194 (2014).
64. Thirumoorthi, M. & Thomas Joseph Prakash, J. Doping effects on physical properties of (1 0 1) oriented tin zinc oxide thin films prepared by nebulizer spray pyrolysis method. *Materials Science and Engineering: B* **248**, 114402 (2019).
65. Mozgin, S. V., Felin, M. G., Subbotina, N. A. & Spitsyn, V. I. Complexes of molybdenum (6) and tungsten (6) with ethanolamines. *Zhurnal Neorganicheskoj Khimii* **27**, 1193–1198 (1982).
66. Homnan, S. *et al.* Low-temperature processable Sn-doped ZnO films as electron transporting layers for perovskite solar cells. *J Mater Sci: Mater Electron* **32**, 27279–27289 (2021).
67. Dhara, S., Niang, K., Flewitt, A., Nathan, A. & Lynch, S. Tail-states induced appearance of conductor-like behaviour in zinc-tin-oxide photo-thinfilm transistors under sub-bandgap light excitation. (2021) doi:10.21203/rs.3.rs-540352/v1.
68. Zatsepin, D. A. *et al.* XPS and DFT study of Sn incorporation into ZnO and $TiO_2$ host matrices by pulsed ion implantation: XPS and DFT study of Sn incorporation into ZnO and $TiO_2$. *Phys. Status Solidi B* **252**, 1890–1896 (2015).
69. Stranick, M. A. & Moskwa, A. SnO2 by XPS. *Surface Science Spectra* **2**, 50–54 (1993).